

Depicting past stress history at passive margins: A combination of calcite twinning and stylolite roughness paleopiezometry in supra-salt Sendji deep carbonates, Lower Congo Basin, west Africa

Aniès Zeboudj^{a,b,*}, Boubacar Bah^a, Olivier Lacombe^a, Nicolas E. Beaudoin^b, Claude Gout^{c,b}, Nicolas Godeau^d, Jean-Pierre Girard^c, Pierre Deschamps^d

^a Institut des Sciences de La Terre de Paris (ISTeP), Sorbonne Université, CNRS-INSU, 75005, Paris, France

^b Université de Pau et des Pays de L'Adour, E2S UPPA, TotalEnergies, CNRS, LFCR, Pau, France

^c TotalEnergies, Centre Scientifique et Technique Jean Féger-CSTJF, Pau, France

^d Aix Marseille Univ, CNRS, IRD, INRAE, CEREGE, Aix-en-Provence, France

ARTICLE INFO

Keywords:

Stress
Paleopiezometry
Calcite twins
Stylolites
Passive margin
Salt

ABSTRACT

The paleostress history and associated deformation mechanisms affecting passive margins are seldom studied, as access to offshore parts is rather limited. We analyze an offshore wellbore core of the Albian, post-rift carbonates of the Sendji Fm which directly overlies the salt of the Aptian Loeme Fm in the Lower Congo Basin. Paleopiezometry based on stylolite roughness inversion (SRIT) and calcite twin inversion (CSIT) was combined with fracture analysis, U–Pb geochronology of calcite cement and burial modeling to unravel the orientations and magnitudes of horizontal and vertical stresses affecting the Sendji Fm over time, with a focus on the impact of salt tectonics on stress records. The results of SRIT on bedding-parallel stylolites constrain the range of depths over which the Sendji Fm strata deformed under a vertical principal stress σ_1 to 650–2800 m (median \sim 1300 m). Once projected onto the burial model derived from TemisFlow™ software, the range of depths converts to a period of pressure solution activity, from 101 to 15 Ma. Calcite twin measurements within the early diagenetic cement (U–Pb age = 101 ± 1 Ma) reveal three main types of stress regimes: (1) extensional stress regimes with σ_3 trending \sim N–S and \sim E–W associated with local, thin-skinned salt tectonics (101–80 Ma), (2) strike-slip stress regimes with σ_1 trending \sim NW–SE to NNE–SSW and a compressional stress regime with σ_1 trending NNW–SSE, reflecting possible intraplate stress transfer from the distant Africa–Eurasia plate boundary (67–60 Ma); (3) a strike-slip and a compressional stress regime with σ_1 trending E–W likely related to the mid-Atlantic ridge push possibly combined with effects of variations in elevation and density of the lithosphere and sedimentary flexural loading (15 Ma to present). The paleostress sequence suggests that the sedimentary cover was decoupled from the crust during salt tectonics and then recoupled from the late Cretaceous onwards.

1. Introduction

Divergent passive margins are diverse in their geometry and structural evolution owing to their segmentation, geodynamic history, and pre-rift inheritance (see review in [Sapin et al., 2021](#)). As a response to continental breakup, they are formed through a process of first rifting and then drifting. Extensional stress prevails during the rifting stage and originates from tectonic forces linked to plate motion, frictional forces exerted by the convecting mantle on the base of the lithosphere (e.g., [Ziegler et al., 1995](#)), asthenospheric flow, basal drag and, to a lesser

extent, from stresses developing in the lithosphere above mantle plumes ([Bott, 1993](#)).

In contrast, the present-day stress field at passive margins is often dominated by a reverse or strike-slip stress regime with maximum horizontal principal stress S_H roughly perpendicular to both the trend of the margin and the oceanic ridge ([Zoback, 1992](#); [Heidbach et al., 2016](#)). This supports the idea that the ridge push may be a possibly significant source of the present-day stress at passive margins (e.g., [Pascal and Cloetingh, 2009](#)). However, the contribution of other gravitational forces should not be neglected. These forces include flexural loading of

* Corresponding author.

E-mail address: anies.zeboudj@sorbonne-universite.fr (A. Zeboudj).

<https://doi.org/10.1016/j.marpetgeo.2023.106219>

Received 1 August 2022; Received in revised form 8 March 2023; Accepted 9 March 2023

Available online 21 March 2023

0264-8172/© 2023 Elsevier Ltd. All rights reserved.

the lithosphere in response to sedimentation or differences in elevation and associated gravitational potential energy differences between the continent and the margin (e.g., [Pascal and Cloetingh, 2009](#)), as well as lateral density differences within the lithosphere (e.g., [Artyushkov, 1973](#); [Zhou and Sandiford, 1992](#)). Finally, when considering the long-lasting post-rift history of passive margins, far-field tectonic stress transfer from distant active plate boundaries may likely have, at least transiently, also played some role ([Ziegler et al., 1995](#); [Withjack et al., 1995](#); [Vågnes et al., 1998](#)).

In the framework of oil exploration, numerous deep supra-salt carbonate reservoirs have been investigated so far along the Atlantic margins ([Brice et al., 1982](#); [Marton et al., 2000](#); [Brownfield and Charpentier, 2006](#)). To date, however, our knowledge on the tectonic and stress evolution of these reservoirs remains limited, especially in poorly accessible offshore domains where well-established paleopiezometry techniques such as calcite twinning paleopiezometry have, to the best of our knowledge, never been applied. The Congolese segment of the Atlantic passive margin of SW Africa exhibits a post-rift salt sequence deposited during the mid-Cretaceous marine transgression associated with slow subsidence ([Moulin, 2003](#)), which triggered gravity-induced thin-skinned extensional salt tectonics and the development of associated structures ([Duval et al., 1992](#); [Gauillier et al., 1993](#); [Penge et al., 1999](#); [Rowan et al., 2022](#)), and therefore significantly increased the structural complexity.

In the proximal margin sequences of the lower Congo basin, the Cretaceous Sendji carbonate formation ([Wonham et al., 2010](#)) presumably recorded the tectonic complexity that can be expected for a supra-salt reservoir. However, the paleoburial and paleostress evolution of this formation remains unconstrained despite being of prime importance for a reliable prediction of its reservoir properties.

In this contribution, we characterize the paleoburial and paleostress evolution of the post-rift, supra-salt Sendji deep carbonate reservoir using a multi-proxy approach. Our method combines calcite twinning and sedimentary stylolite roughness paleopiezometry with fracture analysis, geomechanical tests, U–Pb dating of host rock calcite cement, and burial modeling. We applied this approach to a core recovered from a deep well drilled by Totalenergies in the lower Congo basin. This unique opportunity to better constrain the local paleoburial and paleostress history of a deep offshore reservoir enables us to tackle the question of the origin of stresses that affected the west African passive margin during its long-lasting post-rift geological evolution. Our dataset is also used to illustrate the impact of halokinesis on the stress distribution in a supra-salt reservoir. Beyond the reservoir scale, this study also provides new constraints on the way shallow and deep gravitational and tectonic forces interplay and control the evolution of divergent passive margins.

2. Geodynamic and geological settings

2.1. Geodynamic evolution of the South Atlantic Ocean

The opening history of the South Atlantic Ocean is commonly divided into four major phases: the pre-rift, syn-rift, transitional and post-rift (or drift) phases ([Cainelli and Mohriak, 1999](#); [Beglinger et al., 2012](#)). In the Gondwana supercontinent, from the Late Palaeozoic to the Jurassic, the pre-rift phase was characterized by the development of intracratonic basins and regional sag basins ([Beglinger et al., 2012](#)). During this phase, southwestern Gondwanaland (currently South Africa) was affected by the subduction of the palaeo-Pacific plate beneath the supercontinent ([Lock, 1980](#); [Catuneanu et al., 2005](#)). This compressional regime led to the formation of the PanGondwanian fold-and-thrust belt, now preserved as the Cape Fold Belt in South Africa ([Catuneanu et al., 2005](#)). From the Late Jurassic to the Early Cretaceous, the divergent movement between the future African (Nubian) and South American plates generated the breakup of Western Gondwana. The counter-clockwise rotation of Africa away from South America led to the

progressive northward opening of the South Atlantic ([Heine et al., 2013](#)). The transition phase, starting at the Aptian and ending by the Early Albian, represents a quiescent period when the stretching of the continental crust and related basement-involved fault activity stopped ([Unternehr et al., 2010](#)), starting with an erosional peneplanation period ([Lehner and De Ruiter, 1977](#)). The beginning of the post-rift phase is linked to the onset of the spreading floor between the future African and South-American plates being dated ~112 Ma between latitudes 10°S–27°S (Angola, Congo, and Gabon areas) ([Torsvik et al., 2009](#)). This period was marked by breakup unconformity ([Beglinger et al., 2012](#)). From the Early Albian to the present day, the post-rift phase was characterized by the thermal subsidence of the oceanic lithosphere and the progressive drift apart of the African and South American continents from ~112 to 110 Ma onwards ([Moulin et al., 2010](#)). Noticeably, the Africa motion with respect to Eurasia changed from ENE-directed to NNE-directed during the Campanian then to NNW during the Oligocene ([Guiraud and Bosworth, 1997](#); [Rosenbaum et al., 2002](#); [Jolivet et al., 2016](#)).

2.2. Paleostress and contemporary stress orientations in western Africa

As a consequence of the above described geodynamic evolution, Western Africa underwent a complex tectonic and paleostress history. Stress orientations reported hereafter from the literature refer to the current African plate position.

During the pre-rift phase (280–215 Ma), the southwestern subduction of Gondwana induced an NW–SE compressional stress related to the Gondwanide orogeny ([Johnston, 2000](#)). This was inferred in the Paleozoic Inkisi Group, South West Congo ([Nkodia et al., 2020](#); [Tack et al., 2008](#); [Kadima et al., 2011](#)). From the Late Jurassic to the Early Cretaceous, i.e. during the syn-rift phase, the West African margin experienced a NE–SW oriented extension related to the opening of the Atlantic Ocean ([Rabinowitz and LaBrecque, 1979](#); [Nürnberg and Müller, 1991](#) and [Salomon et al., 2015](#)), also highlighted by [Viola et al. \(2012\)](#) as an ENE–WSW extension.

During the post-rift phase, a major tectonic uplift event took place from Albian to Turonian times (115–90 Ma) on the western coast of South Africa ([Kounov et al., 2009](#)). This uplift induced erosional denudation of up to 2.5–3 km and has been tentatively related to an E–W-oriented extension, recorded on the western coast of South Africa ([Viola et al., 2012](#)). [Viola et al. \(2012\)](#) also recognized two subsequent compressional events, with σ_1 oriented NW–SE and NNE–SSW, respectively, as well as a NE–SW oriented extension in between.

A strike-slip stress regime associated with NW–SE-oriented compression was recognized in Namibia by [Salomon et al. \(2015\)](#) and in continental Congo by [Nkodia et al. \(2020\)](#). In the absence of stratigraphic constraints, these stress regimes could not be precisely dated but were tentatively correlated, based on consistent stress orientations, to the compressional and extensional tectonic events described in Central and North Africa by [Guiraud and Bosworth \(1997\)](#), namely the late Santonian N–S to NW–SE compression, the mid-Campanian–Maastrichtian NE–SW extension and the late Maastrichtian–early Paleocene N–S to NW–SE compression. The authors related these tectonic events to the shift in opening directions of the Atlantic oceanic spreading centers and the subsequent counterclockwise rotational northward drift of Africa–Arabia into Eurasia during the so-called “End Cretaceous event” ([Guiraud and Bosworth, 1997](#); [Guiraud et al., 2005](#)).

From the Miocene onward, [Nkodia et al. \(2020\)](#) reported a consistent ENE–WSW-oriented compression in onshore Congo using inversion of fault-slip data from the Paleozoic Inkisi Group. Although this compression could not be dated, the authors speculated that this ~ E–W compression started in the Miocene and would possibly be related to some degree to the Atlantic ridge push associated with variations of the lithospheric structure and gravitational energy. The overall E–W compressional stress field still prevails in the present-day as established

in the World Stress Map Project (Heidbach et al., 2016) and by inversion of earthquake focal mechanisms in Congo (Delvaux and Barth, 2010).

2.3. Geology of the offshore lower Congo basin

Amid the several rift basins located in the West African passive margin (Fig. 1A), the Lower Congo Basin covers approximately 115,000 km² distributed between Congo and Angola. It is bounded to the north by the South Gabon basin and to the south by the Kwanza basin. The Lower Congo basin is characterized by a succession of stratigraphic mega-sequences as described hereinafter. For the following, we gather under the term ‘basement’ both the crystalline part of the Congo craton and the overlying Precambrian pre-rift sediments (Delpomdor et al., 2008; Mbina Mounquengui and Guiraud, 2009), so the Cretaceous-Cenozoic sedimentary series rests directly on the so-called Precambrian ‘basement’ (Fig. 1B and C). The younger pre-rift sedimentary sequences are missing in the basin (Brownfield and Charpentier, 2006).

The syn-rift megasequence is characterized by two main continental lithofacies: lacustrine black shales and deltaic/fluviol sediments (Baudouy and LeGorjus, 1991; Harris, 2000). The syn-rift sedimentary succession (Fig. 1B) begins with the fluvial and alluvial deposits of the Vandji-Lucula Fm (Bracken, 1994), followed by the lacustrine shale of Sialivakou Fm until about 141 Ma, and by the Djeno sandstone until 130 Ma for a total thickness between 200 and 600 m. The Pointe Noire and Toca formations correspond to lacustrine deposits (clays and limestones respectively) that were deposited until 125 Ma (Chaboureaux et al., 2013). The syn-rift phase ends with the deposition until 118 Ma of the Pointe Indienne Fm./Tchibola Fm made of at least ~270 m thick lacustrine siliciclastic shales. The overall pre-salt sequence - including pre-rift and syn-rift sequences - can reach 5000 m in thickness near Angola (Lehner and De Ruiter, 1977). The transition phase is associated with a megasequence starting with a peneplanation phase followed by ~60 m thick Aptian sandstones of the Chela Fm (Lehner and De Ruiter, 1977) and ends with the massive Aptian evaporite Loeme Fm comprising interbedded anhydrite, halite, and potash salts. The Aptian salt basin spreads along 2000 km from southern Angola to the Cameroon shores and extends up to 250 km offshore. The thickness is very variable, estimated at ~300 m at the basin scale (Ala and Selley, 1997) but can reach locally 1000 m (Lehner and De Ruiter, 1977; Brice et al., 1982). This Aptian salt episode marks the transition between the rifting phase and the subsequent thermal subsidence due to lithosphere cooling following the breakup and oceanic accretion (Brognon and Verrier, 1966; Cainelli and Mohriak, 1999).

The Loeme Fm is overlain by the marine post-rift megasequence, characterized by three supersequences: (1) the restricted marine supersequence made of high energy, shallow-water carbonates, tidal sandstone deposits, and silts (Baudouy and LeGorjus, 1991) followed by shallow and deep marine clastic deposition (Séranne and Anka, 2005; Anka et al., 2010) topped with organic-rich black shales. (2) the open marine supersequence comprises sandstones, shelly limestones, and siltstone, characteristic of the transgression phase during oceanic deposition. (3) the deltaic supersequence is marked by a major submarine erosion of the ramp (McGinnis et al., 1993; Séranne and Anka, 2005).

In summary, the post-rift sedimentary succession (Fig. 1B) started with the ~1000 m thick Sendji Fm limestone, dolomite, sandstone and silts that were deposited between 112 and 99.6 Ma (Fig. 2). This Albian layer was overlain by Cenomanian deposits with an age up to 93.5 Ma, consisting either of the Tchala sandstones that were deposited in a continental to marginal litoral environment in the eastern part of the basin, or of the ~600 m thick Likouala siltstone that was deposited in a marginal litoral environment in the rest of the basin. These Cenomanian formations were covered by the ~200 m thick Madingo marls, with an age up to 34 Ma. The megasequence ended with the ~1800 m thick sandstone and shales of the Paloukou Fm.

2.4. The N’Kossa oil field and the Sendji Formation

2.4.1. Structure

The N’Kossa field is located in the Lower Congo Basin, 60 km off the Congolese coast (Fig. 1A, C). The general structure of the N’Kossa field originated from salt tectonics, defining a major raft structure bounded by compensation normal faults and by long-lasting gravity-related listric normal faults on the western side. Three main stages of structural evolution can be described: (1) the initiation of salt diapirs during the Early Albian, (2) the formation of the local raft structures bounded in the East by N–S to NNW–SSE striking normal faults (Fig. 3) (Rouby et al., 2002; Wonham et al., 2010) and (3) the development of N–S striking listric normal faults (Fig. 3) in response to local E–W extension triggered by the collapse and lateral creep of the underlying salt. The geometries of the post-rift, post-salt formations in the area of the N’Kossa raft are shown on the interpreted seismic profile in Fig. 4 (TotalEnergies internal report). The area of interest comprises a raft structure bounded by two listric faults separating the Albian limestone deposits from the Cenomanian deposits (Fig. 4), with the remaining salt in the footwall of the bounding faults (Rouby et al., 2002). Gravity-related extensional salt tectonics were initiated during Late Albian and intensified due to the increased sediment loading (TotalEnergies internal report).

The salt-related raft tectonics that took place in the N’Kossa field area is widespread recognized along the South Atlantic margin (Duval et al., 1992). Fig. 3 illustrates the structural setting of the top Lower Sendji Fm. Large, multi-kilometer-long, broadly N–S striking normal faults affect the lower Sendji Fm and delineate the N’Kossa field (Fig. 3). Smaller NW–SE-oriented normal faults link these large listric normal faults. This complex fault pattern results from the translation of a raft over a non-planar substrate (in this case, the Loeme Fm).

2.4.2. Stratigraphic succession of the Sendji Formation

The Albian Sendji Fm corresponds to the first stage of the post-salt restricted marine supersequence, and can be divided into two layers (TotalEnergies internal report, Wonham et al., 2010): (1) the Lower Sendji (Early Albian), which corresponds to the reservoir level of the N’Kossa field, and (2) the Upper Sendji (Late Albian). The Lower Sendji comprises shelf and litoral deposits mainly composed of limestones and dolomites, whereas dominant lithologies in the Upper Sendji are sandstones and shales (Wonham et al., 2010). In the N’Kossa field area, four sequences can be recognized in the drill core (Fig. 2) from a reference well located at the top of the N’Kossa raft. At the top of the N’Kossa raft, the first sequence (S1) is characterized by 108 m of dolomite and anhydrite confined deposits. The second sequence (S2), is made up of 114 m of more detrital deposits with a dolomitic front. The third sequence (S3) is a 68 m thick succession marked by flooding, characterized by a strong lithological variation of sandstone, dolomitic sandstone, limestone, dolomite alternation, and very fine clay levels. This sequence corresponds to the hydrocarbon reservoir section of the Sendji Fm. Opening and deepening of the depositional environment are characterized by the last sequence (S4), a sequence of alternating limestones, sandstones, and minor silty clays, forming the reservoir seal.

From base to top, the depositional environments evolved as follows: an upper infralittoral environment marked by the presence of arenaceous foraminifera in a predominantly wackestone series, a supralittoral stage characterized by a siltic-dolomitic series with anhydrite that becomes more dolomitic upward the core, a lower infralittoral to an upper infralittoral environment characterized by a wackestone series followed by an upper circalittoral stage. The depositional environment analyses indicate a bathymetric deepening with time during Albian. All the analyzed facies indicate an internal platform deposit environment (TotalEnergies internal report). Gravely facies indicate an upper subtidal environment with low porosity (0–5%), while the oolitic facies indicate a lower subtidal environment with greater porosity (5–10%).

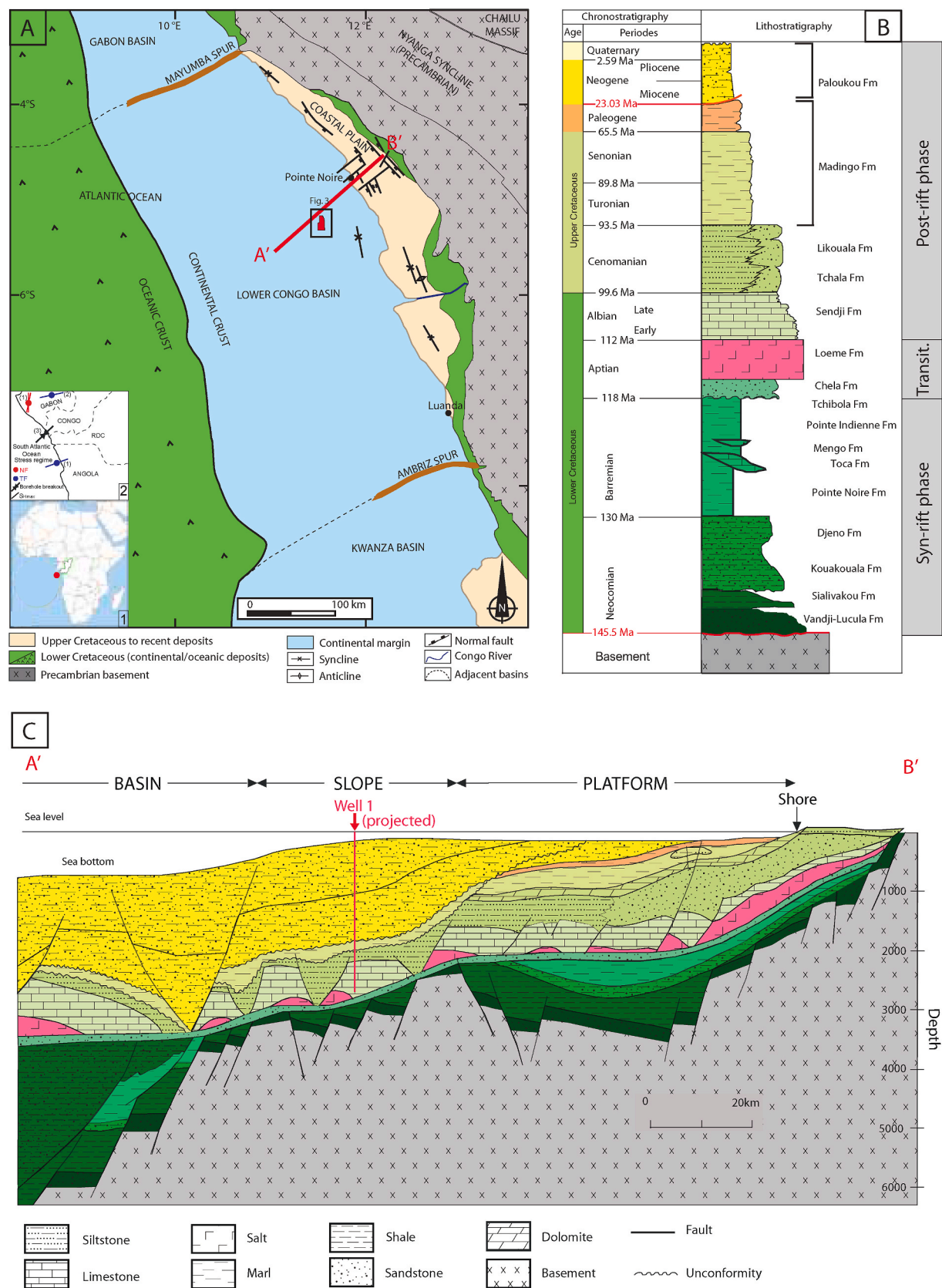


Fig. 1. A. Simplified geological map of the Lower Congo Basin area, offshore Republic of Congo. B. Stratigraphic column of the Lower Congo Basin (modified from TotalEnergies internal report). C. Cross section of the Lower Congo Basin with the horizontal projection of well 1 (modified from Brownfield and Charpentier, 2006).

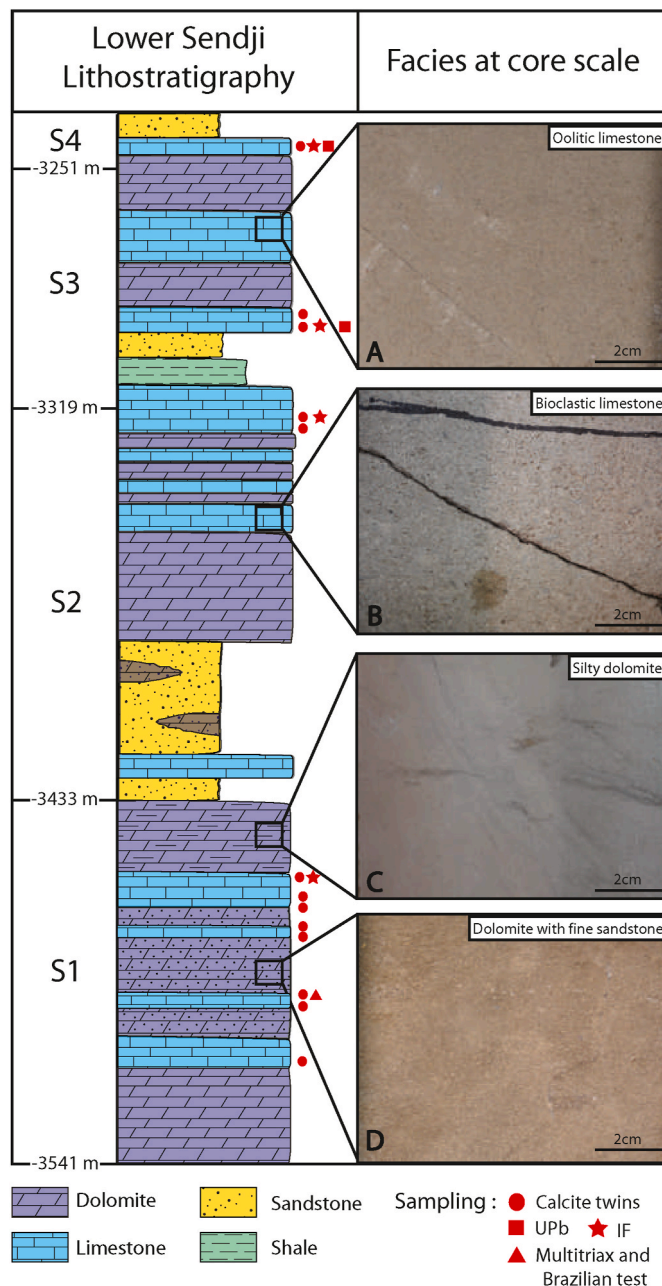


Fig. 2. Lithostratigraphy of the Lower Sendji formation with successive sequences and the associated facies from discontinuous core sections analyses completed by the TotalEnergies database. A. Oolitic limestone. B. Bioclastic limestone. C. Silty dolomite. D. Dolomite with fine sandstone.

3. Material

This study is based on the analysis of a continuous core of 306 m (–3235 to –3541 m BSW) of the Lower Sendji Fm recovered from Well 1 in the N’Kossa raft (Fig. 3). The core is slightly deviated with respect to the vertical axis, up to 5° in places. The orientation of the drill core was determined after drilling by comparing the FMS (Formation Micro-Scanner) imagery recorded on the borehole with the core images. It was thus possible to find the orientation of fractures or bedding of the non-oriented core by comparing the same fractures and bedding oriented by FMS present in the well.

The cored interval of the Sendji Fm represents the reservoir part and internal platform deposits (dolomite, sandstone, and limestone). The main facies in the core are shown in Fig. 2, such as oolitic limestone,

bioclastic limestone, silty dolomite, and dolomite with fine sandstone. Limestone levels are particularly rich in stylolites and display sparry crystals suitable for calcite twin analysis. The investigation, therefore, focused on the gravelly and bioclastic-oolitic limestone facies. It is noteworthy that Well 1 is located close to the intersection between two normal faults above the top Sendji Fm (Fig. 3).

4. Methods

We adopted an original combination of methods to constrain the burial and paleostress history of the Sendji Fm. First, petrographic studies and U–Pb geochronology were used to identify the nature and to constrain the absolute age of the main calcite cement, respectively. Fluid inclusion microthermometry applied on these cements reveals the minimum temperature of the fluid from which it precipitated. Second, the inversion of sedimentary stylolite roughness combined with the elastic parameters of the carbonates derived from mechanical tests constrains the depth of active, compaction-related pressure solution under a vertical σ_1 . Third, the inversion of calcite mechanical twins from the main cement is used to determine the orientations and the magnitudes of the stresses that were recorded by the Sendji Fm since its deposition. Then the time periods of prevailing either compaction-dominated or salt tectonics-related vertical σ_1 on the one hand, and of prevailing tectonic-related horizontal σ_1 on the other hand, can be determined by combining the above stress results with time-burial modeling. Results of calcite twin inversion are finally further combined with the rock strength envelope derived from the mechanical tests to interpret and predict fracture occurrence in the Sendji Fm.

4.1. Petrographic analyses of calcite cement

To establish the paragenesis and diagenetic sequences of the Well 1 samples, a petro-diagenetic study was carried out on 39 thin sections. Optical petrography was conducted using a Zeiss Axiophot polarizing microscope equipped with a Nikon Digital sight DS_U2/Ds_Fi1 camera at the CSTJF TotalEnergies in Pau. The petrographic phases were identified in LPNA (unanalyzed polarized light) and LPA (analyzed polarized light), then the diagenetic sequence was investigated using cathodoluminescence on a NewTec scientific Cathodyne model CATHOD-SP01 equipped with a cold cathode and an IDS camera UI-3850CP-C-GL. These analyses were performed with replicable parameters, 90 mTorr vacuum, 12–15 kV voltage, and 200 μ A electron beam.

4.2. U–Pb geochronology of calcite cement

The absolute dating of the main calcite cement was carried out at Centre Européen de Recherche et d’Enseignement des Géosciences de l’Environnement (CEREGE), Aix-en-Provence, France. The equipment consists of an ArF 193 nm excimer laser (ESI, Elemental Scientific Industries) coupled to an HR-ICP-MS (High Resolution Inductively Coupled Plasma Mass Spectrometry) with magnetic sector (Element XR, Thermo fisher). Measurements were performed following a methodology analogous to Godeau et al. (2018). Analyses were carried out directly on polished 100 μ m thick sections. Samples were first scanned with a resolution of 3200 dpi to pre-select the areas of interest, i.e. consisting of calcite cement from the same diagenetic phase. The samples were first screened to assess the quality of the U–Pb signal (U and Pb intensity, variability of the U–Pb ratio) and to identify the best spots to perform the analysis (Roberts et al., 2020). The ESI laser beam was configured as follows: 150 μ m spot-size, 193 μ m wavelength, and 10 Hz firing rate. The energy of the laser was adapted to carbonates, i.e. with a density of the photon emitted per surface density of 1–1.3 J/cm². To obtain good statistics and a robust age, we usually performed ~30 spots per mineral phase to be dated. During analysis, the ablation speed was of the order of 1–1.5 μ m/s under standard conditions, following a pre-ablation phase of a few seconds to clean the sample surface.

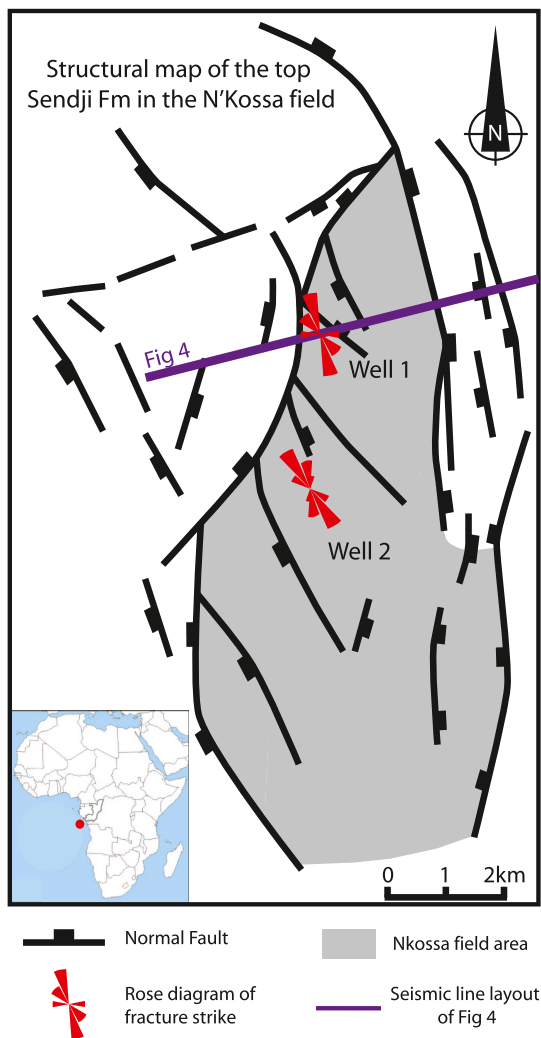


Fig. 3. Structural map of the top of the Sendji Fm in the N'kossa field (modified from TotalEnergies internal report).

Correction of the instrumental bias was done using the WC-1 natural calcite standard for inter-elemental fractionation (reference age = 254.4 ± 6.4 Ma; Roberts et al., 2020). The U–Pb isochron age was established from Tera–Wasserburg plots constructed using the Isotplot 4.15 add-on (Excel™).

4.3. Fluid inclusion microthermometry

Four double-polished 150 μm thick wafers, distributed along the drill core, were used for microthermometric analysis of fluid inclusions. Fluid inclusions are small cavities or pores, typically ranging from micrometer to millimeter size, filled with fluid, ubiquitously found in minerals, which can provide information on the nature and the trapping temperature of the mineralizing fluid (Goldstein and Reynolds, 1994). The micro thermometric study was performed by H-Expertise services, Nancy France. The selection of aqueous primary fluid inclusions was based on a petrographic study based on optical observations by polarized light and epi-UV fluorescence. The epi-UV fluorescence observations were conducted using a Zeiss Axiolmager.A1m microscope with an excitation filter centered at 365 ± 5 nm and an emission filter long pass around 400 nm.

Samples were first heated to reach their homogenization temperature, i.e. T_h , then they were cooled down to ice freezing and heated up again to reach the final melting temperature of ice, i.e. $T_{m(\text{ice})}$. These phase transitions were measured at temperatures between -170 °C and 400 °C using a LINKAM MDS 600 heating-freezing stage equipped with a Sony Exwave HAD3 color video camera mounted on an Olympus BX 51 microscope at GeoRessources laboratory (Nancy, France). The microthermometric stage was thermally calibrated using CO_2 synthetic fluid inclusions standards for $T_{m(\text{CO}_2)}$, H_2O synthetic fluid inclusions standards for the final melting temperature of ice, $T_{m(\text{ice})}$, and cross-calibrated natural alpine fluid inclusions (Georessources standard) for the bulk homogenization temperature T_h . The accuracy of measurements is estimated at ± 0.2 °C for $T_{m(\text{ice})}$ (heating at $0.5\text{--}1$ °C/min) and ± 0.5 °C for T_h (heating at $1\text{--}5$ °C/min).

4.4. Rock mechanical properties

Mechanical properties of the limestone levels of the Sendji Fm were characterized by multiaxial tests and Brazilian tests. The multiaxial, or

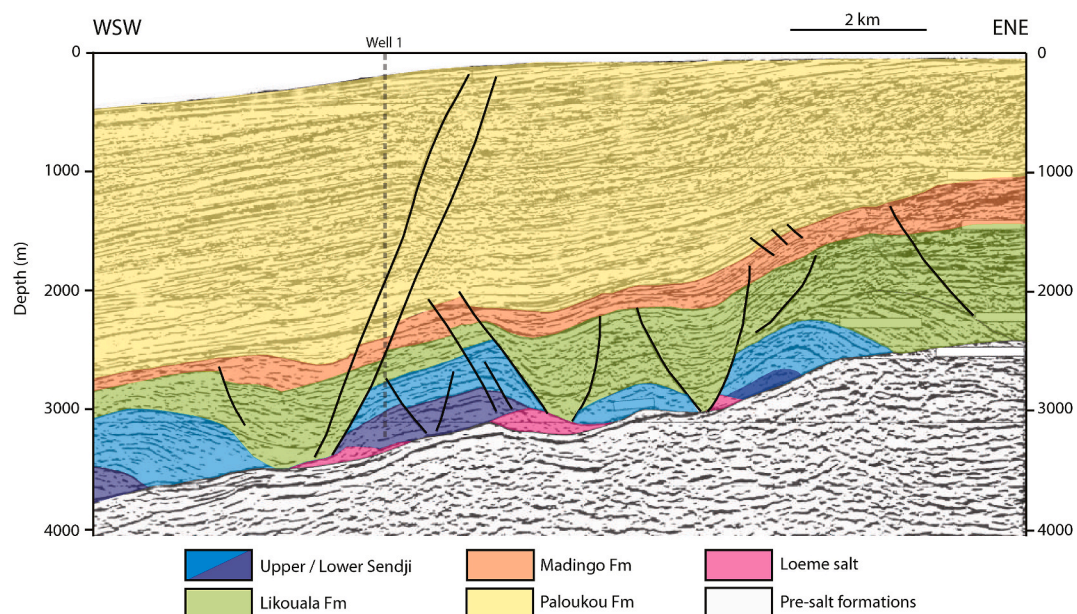


Fig. 4. Interpreted seismic profile of the N'kossa field area (modified from TotalEnergies internal report).

multi-stage test, consists of a triaxial revolution test during which confining pressure is fixed and the sample is brought close to failure. Soon before failure occurs, the confining pressure is increased so it precludes failure. The cycle is repeated 3–4 times, which enables to simulate a maximum of triaxial tests with a single sample. The tests were carried out at the Geomechanical Laboratory located at the Total-Energies CSTJF (Pau, France). Two plugs (38 mm diameter x76 mm height) were selected to be representative of stylolite-bearing lithologies, i. e. limestone then were cut along the vertical axis of the core. Each plug was loaded at 10, 30, and 50 MPa of confining pressure. For each confining pressure value, an axial stress ramp was applied with a displacement rate of 0.01 mm/min until the yield point was reached, then the deviatoric stress was unloaded with the same displacement rate at 0.01 mm/min to finalize the cycle.

The values of the maximum principal stress (σ_1) at 10 MPa and 30 MPa have been used to build the Mohr circles. For that, the yield stress, also known as the applied stress at which irreversible plastic deformation is first observed and the end of the elastic behavior, was multiplied by the ratio between the yield stress at 50 MPa and the maximum stress at 50 MPa. Following the Mohr-Coulomb criterion, Mohr circles associated with each loading enabled us to build the failure envelope that was approximated by a straight line in the domain of positive normal stress, characterized by the following equation:

$$|\tau| = S_0 + \mu \sigma_n$$

with the shear stress component τ , the cohesion of the material S_0 , the coefficient of internal friction, μ , and the normal stress component σ_n . Deformation was measured by axial and radial gauges, and the elastic parameters (Young modulus, Poisson ratio) were determined along with the friction angle, cohesion, and maximum strength of the rock sample.

The diametral compression (or Brazilian) tests were performed to evaluate the indirect tensile strength of the rock. A thin disc sample was placed in a specially designed cell consisting of two steel parts assembled

with the sample in the middle. The load was continuously increased at a constant rate until the failure of the sample occurs.

4.5. Sedimentary stylolite analysis

4.5.1. Morphology and distribution of stylolites

Stylolites are localized rough dissolution surfaces common in carbonate formations. Stylolites form as a result of pressure-solution related to either vertical, compaction-related stress (sedimentary stylolites) or tectonic stress (tectonic stylolites). Stylolites affect the petrophysics of the reservoir by reducing porosity (Raynaud and Carrio-Schaffhauser, 1992; Ehrenberg, 2006) and permeability when insoluble material such as clays plays a sealing role (e.g. Koehn et al., 2016), albeit stylolites can also be localized conduits for fluids (Martín-Martín et al., 2018; Koehn et al., 2016; Gomez-Rivas et al., 2022). Stylolites can be classified into four types of morphologies (Koehn et al., 2016, Fig. 5): (1) class 1 (rectangular layer) is characterized by a rectangular baseline with peaks on the rectangle flat top. (2) Class 2 (Seismogram pinning) is characterized by small-scale pics on top of narrow rectangle large-scale teeth. (3) Class 3 (Suture/sharp peak) is characterized by a flat or wavy baseline and locally tall peaks. (4) Class 4 (Simple wave-like) is characterized by a simple wave baseline. The minimum value of the compaction (or vertical displacement) accommodated by a stylolite can be estimated in the first order by measuring the maximum amplitude of the teeth (Koehn et al., 2016; Toussaint et al., 2018). A statistical analysis of the distribution of these stylolite classes was carried out to reveal a possible lithological control and to study their density in order to highlight isolated stylolites or clusters. For each stylolite, we have reported the depth in the core and the class the stylolite belongs to. These data were completed with data previously collected by Total-Energies for the core intervals we did not have direct access.

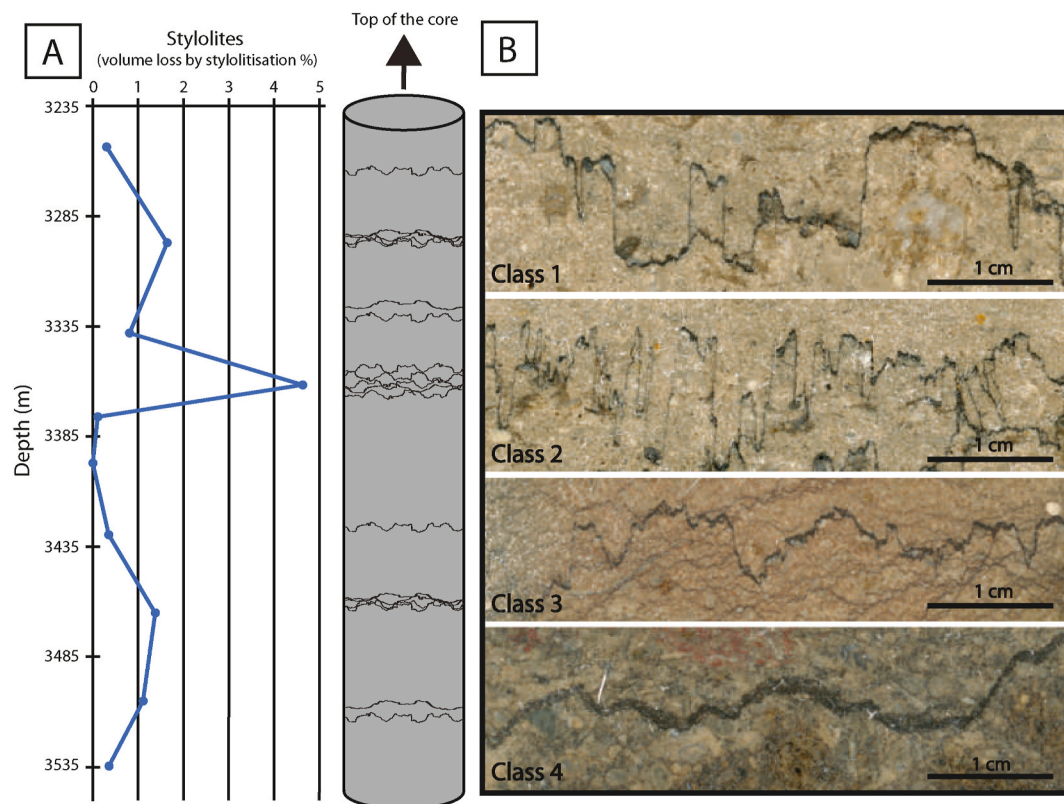


Fig. 5. A. Volume loss by stylolitisation showing the distribution of bedding-parallel (sedimentary) stylolites along the drill core (analyses completed by the TotalEnergies database). B. Stylolite morphology classes.

4.5.2. Stress inversion of sedimentary stylolite roughness

The recent development of stress inversion based on stylolite roughness signal offers a new opportunity to reconstruct the history of vertical stress regardless of the past geothermal gradient and fluid pressure (Schmittbuhl et al., 2004; Ebner et al., 2009, 2010; Toussaint et al., 2018; Beaudoin and Lacombe, 2018; Beaudoin et al., 2019, 2020b). The principle of the inversion of stylolite roughness for stress is based on the idea that the final roughness of a stylolite, i.e. the difference in height between two consecutive points separated by a set length of observation, is directly related to stress. Bedding-parallel (sedimentary) stylolites (BPS, hereinafter) have been used as paleopiezometers to constrain the maximum depth of active compaction-related pressure-solution in carbonate rocks (Schmittbuhl et al., 2004; Rolland et al., 2012; Koehn et al., 2012; Bertotti et al., 2017; Beaudoin et al., 2019, 2020a; Labeur et al., 2021; Koehn et al., 2022; Bah et al., 2023), leading to recent attempts to time the period at which the vertical stress became lower than the horizontal stress (Beaudoin et al., 2020a, 2020b; Labeur et al., 2021; Lacombe et al., 2021b). This approach relies on the assumption that in a contractional setting, the prime reason that makes a population of BPS stops their development is that the maximum principal stress becomes horizontal. Such an assumption leads to estimating an absolute age that can be attributed to the onset of layer parallel shortening (LPS). In published studies, the obtained age was compared to e.g. U–Pb absolute ages of the LPS-related vein cement, supporting that no BPS developed after the formation of the oldest LPS-related vein (Beaudoin et al., 2020a).

SRIT is a paleopiezometric technique developed by Schmittbuhl et al. (2004) that relies on the self-affine properties of the stylolite final roughness, acquired quasi instantaneously with regard to the geological time scale (~200 years, Aharonov and Katsman, 2009). Indeed, the spatial transform of the signal defined by the roughness of a stylolite along its track can be defined by a power law characterized by a roughness coefficient, the so-called Hurst exponent (Barabási and Stanley, 1995), that is a constant for a given process. For example, considering a Fourier Power Spectrum (FPS) transform, the power law is defined by $P(k) \sim k^{-1-2H}$ (1) with $P(k)$ the power, H is the Hurst coefficient, and k the wavenumber (mm^{-1}) (Renard et al., 2004). For stylolites, the roughness can be defined by two self-affine regimes, hence by two different Hurst exponents (Schmittbuhl et al., 2004): the Hurst exponent equals 0.5 at the large scale (typically >1 mm), a value typical of the elastic energy, while it equals 1.1 at a smaller scale (typically <1 mm), suggesting an effect of the surface energy (Schmittbuhl et al., 2004).

Sample preparation consists in cutting the stylolite along two orthogonal faces, both perpendicular to the stylolite plane. Each face is then polished and scanned in 2D with a 12,800 dpi resolution, the 2D track is digitized, then its average trend is set horizontally and to a value of 0. A nonlinear regression with two set slopes corresponding to the Hurst exponents (0.5 and 1.1) is used with regularly binned FPS data to find the L_c value, with an intrinsic uncertainty of ~23% (Rolland et al., 2014).

In the specific case of sedimentary stylolites, i.e., when the magnitude of the in-plane stress can be considered isotropic and smaller than the magnitude of the vertical stress (uniaxial strain hypothesis), the relationship between the cross-over length (noted L_c in m) and vertical stress magnitudes are expressed as:

$$\sigma_v^2 = \frac{\gamma E}{\alpha L_c} \quad (2)$$

with γ the energy of the solid-fluid interface (Jm^{-2}), E young's modulus (Pa), and $\alpha = \frac{(1-2\nu)(1+\nu)^2}{30\pi(1-\nu)^2}$, a dimensionless constant with ν being the Poisson ratio (Ebner et al., 2009). It is noteworthy that the validity of the uniaxial strain hypothesis ($\sigma_v > \sigma_H = \sigma_h$) can be tested by comparing the L_c obtained from the 2 perpendicular cuts, which should be similar within methodological uncertainty. The uncertainty for γ is negligible

and the one for α is very low considering the limited range of variations of the Poisson ratio in carbonates. However, the value of E can be very different among carbonates, and it weighs more than the other parameters in equation (2). Its calibration by mechanical tests, therefore, allows for reducing considerably this uncertainty, which can be considered then as negligible. Then, the 23% uncertainty on the value of L_c is the main source of uncertainty in the calculation of σ_v . Considering equation (2) that links σ_v to the square root of L_c , the final uncertainty on the calculated magnitude of σ_v amounts to 12% (Rolland et al., 2014).

The maximum depth at which the stylolite stopped being active is obtained by the following equation:

$$\sigma_v = \rho gh \quad (3)$$

with ρ the density of the rock column above the stylolite (g.m^{-3}), g the gravitational field acceleration (m.s^{-2}), and h the depth at which the dissolution along the stylolite halted (m). Noticeably, since the chemo-mechanical model assumed for SRIT considers that the dissolution occurs on a pressurized plane at the fluid-rock interface (Toussaint et al., 2018), the conversion of σ_v into depth is independent on surrounding fluid pressure, then it is sound to consider the dry density of the rock column for the value of ρ (Ebner et al., 2009). When applied to a population of BPS, SRIT yields the range of depths in which compaction-induced pressure solution was active under a vertical maximum principal stress (e.g. Beaudoin et al., 2019; Labeur et al., 2021) even though some local fluid pressure effect might also halt pressure solution at depth (e.g. Bah et al., 2023).

4.6. Calcite twin analysis

4.6.1. Calcite twin data acquisition

From each sample, three mutually perpendicular thin sections of well-defined orientation in the core (X axis parallel to the generator of the oriented core, Y the dip of the core and Z the normal to the XY plane) were analyzed. For each crystal, the strike and dip of the twinned and untwinned planes were measured using an optical microscope equipped with a Universal stage and with the help of the software of Tournieret and Laurent, 1990). About 30 crystals were measured on average in each of the 3 thin sections, for a given sample. Moreover, orientations of optical axes and poles to twinned and untwinned planes were projected into the geographical referential to ensure a random spatial distribution within each sample. We also ensured that calcite twins were collected from grains belonging to the same diagenetic phase based on cathodoluminescence images.

In order to have a rough estimate of the strain accommodated by twinning, we summed the width of each twin lamella of a given twin set in grain and divided this value by the width of the grain measured perpendicular to the twins. The grain size was determined as (long-axis + short axis)/2 in 2D (thin sections) for each grain and the representative range of grain sizes for each sample was determined from a grain size histogram by eliminating the smallest and/or largest crystals, which are under-represented. The mean grain size and internal strain were further used to constrain the value of the Critical Resolved Shear Stress for twinning (Parlangeau et al., 2019) to be used in the inversion process (Lacombe et al., 2021a).

4.6.2. Stress inversion of calcite twins

Calcite twins (e.g., Jamison and Spang, 1976; Lacombe and Laurent, 1992; Lacombe, 2007) are a well-established paleopiezometer that has been successfully applied to quantify paleostresses in intracratonic and foreland sedimentary basins as well as in fold-and-thrust belts (e.g., Lacombe et al., 1990, 1993, 2007; Rocher et al., 1996, 2000; Craddock et al., 1993; Kulikowski and Amrouch, 2017; Beaudoin et al., 2022. See Lacombe, 2010 and Lacombe et al., 2021a for reviews). Mechanical twinning is a common mechanism of plastic deformation in calcite

crystals (Fig. 6A) at low pressure and temperature (Tournet and Laurent, 1990; Lacombe et al., 1990; Burkhard, 1993 Ferrill et al., 2004; Lacombe et al., 2021a). Twinning occurs by an approximation to simple shear in a particular direction and sense along specific crystallographic e planes (Fig. 6B). The effect of strain rate, temperature, and confining pressure is negligible on twinning activation, the latter being mainly dependent on differential stress, grain size and strain (Rowe and Rutter, 1990; Lacombe et al., 2021a). Twinning occurs if the resolved shear stress τ_s exceeds or equals the critical resolved shear stress τ_a (or CRSS) (Jamison and Spang, 1976; Tullis, 1980; Lacombe and Laurent, 1996; Lacombe, 2010; Lacombe et al., 2021a): the e -twin plane is twinned if and only if $\tau_s \geq \tau_a$, and remains untwinned if $\tau_s < \tau_a$. τ_a decreases with increasing grain size and increases with the amount of accommodated strain since calcite hardens once twinned (Turner et al., 1954; Rowe and Rutter, 1990; Laurent et al., 2000; Lacombe, 2010; Parlangau et al., 2019; Lacombe et al., 2021a).

In order to determine the successive paleostress tensors from the measured twin dataset, we used the stress inversion technique (CSIT-2) developed by Parlangau et al. (2018). The principle of the inversion is to find the different stress tensors which theoretically satisfy the inequalities between τ_s and τ_a for several measured twinned planes and the whole set of untwinned planes. Each stress tensor solution has the form of a reduced stress tensor with 4 parameters: the orientation of the principal stress axes (σ_1 , σ_2 , σ_3), and the stress ratio ϕ .

$$1 \geq \phi = \frac{\sigma_2 - \sigma_3}{\sigma_1 - \sigma_3} \geq 0 \quad \text{with} \quad \sigma_1 \geq \sigma_2 \geq \sigma_3 \quad (4)$$

CSIT-2 first applies several thousands of reduced stress tensors determined by the systematic scanning of the 3D orientation space (with the 3 Euler's angles being sampled every 10°) and with a stress ratio of 0.5 on the set of twinned and untwinned planes, and selects those tensors which account for at least 20% of the set of twinned planes. For each of these tensors, a penalization function is defined as:

$$f = \sum_{j=1}^{j=n} (\tau_s^j - \tau_s^{\min}) \quad (5)$$

with τ_s^j the resolved shear stress applied on the j untwinned planes such as $\tau_s^j \geq \tau_s^{\min}$ and τ_s^{\min} the smallest resolved shear stress applied on the twinned planes compatible with the tensor. The penalization function should theoretically equal 0 for a perfect dataset and increases if incompatible untwinned planes are incorporated into the solution. The stress tensors with a penalization function lower than 0.5 were retained and each of them was weighted by the number of its nearest neighbors based on a similarity criterion. This allows the simultaneous and automatic detection of the few different clusters of tensors that share a high percentage of accounted twinned planes and which are associated with

low values of the penalization function. The reference reduced stress tensor of each cluster is then applied to the set of twinned and untwinned planes while the percentage of twinned planes to be explained is progressively increased. The final solution tensor is the one for which the number of compatible twinned and untwinned planes is maximum, while the value of the penalization function remains low (ideally less than 1) (see Parlangau et al., 2018 for details).

For each stress tensor, the inversion process yields the orientation of the principal stress axes, the stress ratio, and non-dimensional differential stress $\frac{(\sigma_1 - \sigma_3)}{\tau_a}$ which is related to the final value of τ_s^{\min} :

$$\frac{(\sigma_1 - \sigma_3)}{\tau_a} = \frac{1}{\tau_s^{\min}} \quad (6)$$

The suitable value of the CRSS τ_a is determined as a function of grain size (Newman, 1994; Covey-Crump et al., 2017; Meyers et al., 2001) and strain (Turner et al., 1954; Laurent et al., 2000; Lacombe, 2010) using the curves reported in Lacombe et al. (2021a). Knowing the value of τ_a (in Pa) and τ_s^{\min} , the actual differential stress value ($\sigma_1 - \sigma_3$) can be determined using equation (6). The methodological uncertainties are

$\pm 10^\circ$ for the principal stress orientations, ± 0.1 for the stress ratio and

$\pm 30\%$ for $(\sigma_1 - \sigma_3)$. The ability of this technique to detect, separate and determine stress tensors from monophase and polyphase twin datasets, including measurement errors or various grain sizes, has been demonstrated by multiple tests on numerically generated twin datasets as well as naturally deformed polyphase samples (Parlangau et al., 2018).

4.7. Fracture analysis

Fracture orientation data were collected from the cored Sendji interval. Fractures were either reoriented using fracture picking on Formation Micro-Scanner (FMS) or directly measured on the core. For the first method, the FMS processing and high-resolution core images were compared to reorient the fractures. The second method consisted of measuring the fractures directly on the core with a compass equipped with a dipmeter, positioning the generator to the North, then correcting from the actual orientation of the generator. When possible, the deformation mode of fractures (opening or shearing) was determined to ensure that the opening mode corresponds to an opening perpendicular to the vein (or fracture) and the shearing mode corresponds to a lateral displacement of the matrix. These observations are made in 2D therefore we remain careful about the attribution of these deformation modes. Depending on their orientation and deformation mode, the formation and the kinematics of the fracture sets were related to the activity of the major faults and/or to the stress regimes reconstructed from calcite twins.

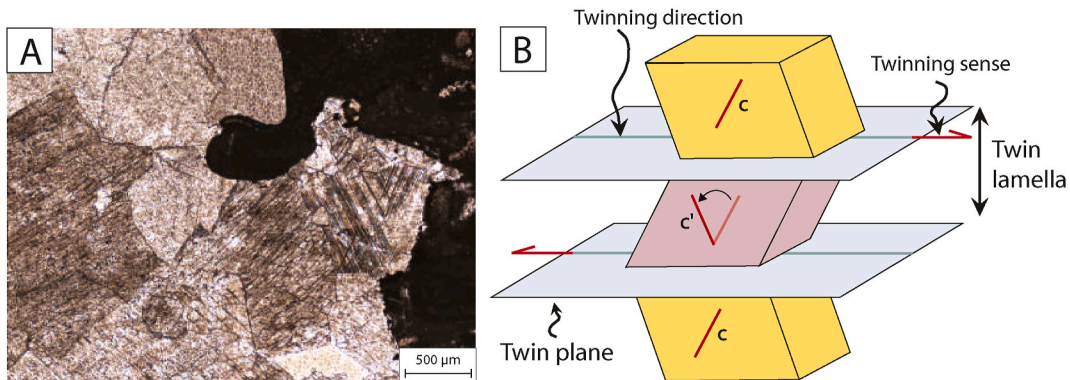


Fig. 6. A. Photograph in natural light of twinned calcite grains. B. Schematic representation of calcite twinning with C the optical axis of the host and C' the optical axis of the twinned portion of the crystal (Lacombe et al., 2021a).

4.8. Construction of a burial model

Petroleum system modeling software TemisFlow™ was used to generate a burial model applying a backstripping process (Perrier and Quiblier, 1974). Backstripping consists in removing the successive sedimentary layers and decompacting the remaining layers to reconstruct the thickness of the strata at each time step since they are deposited.

Lithological data and depths of the top and bottom of each formation we obtained from a nearby well (located 1 km from well-1). This well includes more complete information than well-1 and the geological events (erosion) was described from the seismic reflection image interpretation (TotalEnergies unpublished maps). The chronostratigraphic column (Table 1) is composed of a list of layers (14 for this study, corresponding to the main formations), each of these layers being characterized by a number, a beginning age, and an ending age. Restored geometries can be edited by defining erosion thickness and paleo topography or paleo bathymetry at each time step. Each layer was defined by the ratio of the different sedimentary facies (limestone, shale, sandstone) from which petrophysical parameters such as initial porosity, solid density, and permeability are defined.

The backstripping process was based on the input data described above. This step begins with the computation from present-day to –145.5 Ma when only the substratum remains. For each event (deposition or erosion) every formation is progressively removed or eroded layers are added. Once sedimentation and erosion are accounted for, the remaining sediments are decompacted, or compacted (if eroded or not), using the porosity/depth relationships for each lithology that make up the 1D block through the forward modeling. Porosity is a variable parameter during burial and is related to the conventional hydrostatic exponential compaction laws for each lithology.

5. Results

5.1. Sedimentologic and diagenetic evolution

Four main sedimentary facies were recognized in the studied core interval (Fig. 7). The first facies corresponds to a grainstone-packstone with oolites and bioclasts (Fig. 7A) which is interpreted to have been deposited in a tidal flat of upper infralittoral to supralittoral environment with episodic emersion. These facies are characterized by cemented shells as is the case for the second facies, a micritic matrix wackestone with bioclasts (Fig. 7B). This limestone was deposited in the internal part of the oolite-dominated tidal bars of the upper infralittoral

Table 1

Input data used in the burial model construction (using TemisFlow). Parameters such as age, thickness, and initial porosity of each syn-rift and post-rift formations are indicated.

Event		Age (Ma)		Thickness (m)	Initial Porosity %
Name	Number	From	To		
Paloukou	14	33.9	0.0	1833.9	60
Erosion	13	65.5	33.9		
Lower Tertiary	12	65.5	33.9		
Madingo	11	93.5	65.5	207.0	60
Likouala	10	99.6	93.5	605.8	48
Upper Sendji	9	103.0	99.6	417.2	56
Lower Sendji	8	112.0	103.0	527.9	54
Loeme	7	116.0	112.0	60.0	9
Chela sandstones	6	118.0	116.0	45.0	62
Erosion	5	118.0	117.0		
Pointe Indienne shales	4	123.0	118.0	90.0	62
Toca/Pointe-Noire marls	3	130.0	123.0	129.0	51
Djeno sandstones	2	141.0	130.0	117.0	51
Basal sandstones	1	145.5	141.0	90.0	51

environment. Fig. 7C shows a silt-rich dolomite with calcitic and dolomitic cementation from a border of estuarine channels of a restricted domain. The last facies is silto-bioclastic dolomite with clay stringers (in blue in Fig. 7D) and corresponds to a tidal flat of upper infralittoral environment. The diagenetic evolution of the carbonate layers includes three main episodes: dolomitization, grain leaching, and calcite cementation. The latter episode consists mainly of the precipitation of a single sparry calcite cement that fills and/or replaces bioclast shells, which is the carbonate phase focused on in this work. (Fig. 7E and F). This cement exhibits a characteristic bright yellow cathodoluminescence, in strong contrast with the surrounding matrix showing dull orange luminescence (See Fig. 7F).

5.2. Absolute U–Pb age dating

Five samples of the sparitic cement filling the micro-shells were selected at depths between 3245.9 and 3469.75 m for U–Pb absolute dating (see location on Fig. 2). Three of these samples could not be dated because the volume of the calcite phase of interest was not sufficient (3469.75 m) or because the U concentration was too low (3454.69 m; 3323.52 m). The two samples collected at 3294.35 m and 3245.9 m depth yielded reliable ages of $100.4 \text{ Ma} \pm 1.6$ and $101.4 \text{ Ma} \pm 0.6$, respectively (Fig. 8).

5.3. Fluid inclusion microthermometry

The ice melting and/or the homogenization temperatures were measured in 112 primary aqueous fluid inclusions in the calci-sparite cement at 3245.90 m, 3294.35 m, 3323.52 m, and 3454.69 m depth (see Fig. 2). All samples showed primary aqueous inclusions that are small to medium in size ($\pm 3\text{--}20 \mu\text{m}$), mostly two-phase ($L_w > V$). Homogenization temperatures of all samples are plotted together in a single histogram in Fig. 9A because the different samples show very similar T_h modes ($T_h = 95^\circ\text{C}$ at 3245 m and 3294 m and $T_h = 90^\circ\text{C}$ at 3323 m and 3454 m). The overall distribution of T_h is unimodal with a median at 90°C , well lower than the current temperature at sample depths (about 3300 m) (ca. 145°C , TotalEnergies internal report) indicating no resetting of the fluid inclusions. Ice melting temperature $T_{m(\text{ice})}$ ranges from -23.2°C to -18.6°C corresponding to high salinities, around 300–320 g/L (range is 21.6 – 24.5 wt % NaCl eq) (Fig. 9B).

5.4. Rock mechanical properties

Mechanical tests yielded three measurements of the elastic parameters at increasing confining stress, i.e. values of 22.7 GPa, 25.2 GPa, and 27.5 GPa for the Young Modulus (E); and values of 0.23, 0.24, and 0.24 for the Poisson ratio (ν). Considering the uncertainties on the determination of the Young modulus and Poisson ratios, of 10% and 20%, respectively, all values were considered to be consistent and the elastic parameters were averaged such as follows: $E = 25 \text{ GPa}$ and $\nu = 0.24$. For the studied sample, the yield stress is 110 MPa (Table 2), and the maximum stress is 130 MPa, so the ratio is 1.18. The calculated values of the rock mechanical parameters are then 20.5° for the friction angle and 9.8 MPa for the cohesion. In the domain of negative normal stress, we used the results of the Brazilian test which indicates that the rock tensile strength is $\sim 3.1 \text{ MPa}$.

5.5. Stylolite distribution and inversion of stylolite roughness for stress

5.5.1. Stylolite morphology and distribution

A total of 52 stylolites were identified and measured over an interval from 3245 m to 3493 m. Observations of stylolite morphology reveal the predominance of class 3 (61% of the stylolites), then of class 2 (27% of the stylolites). Classes 1 and 4 are the least represented, they are associated with 7 and 5% of the stylolites, respectively. Overall, the distribution of stylolites is rather uniform with an average of 2 stylolites per

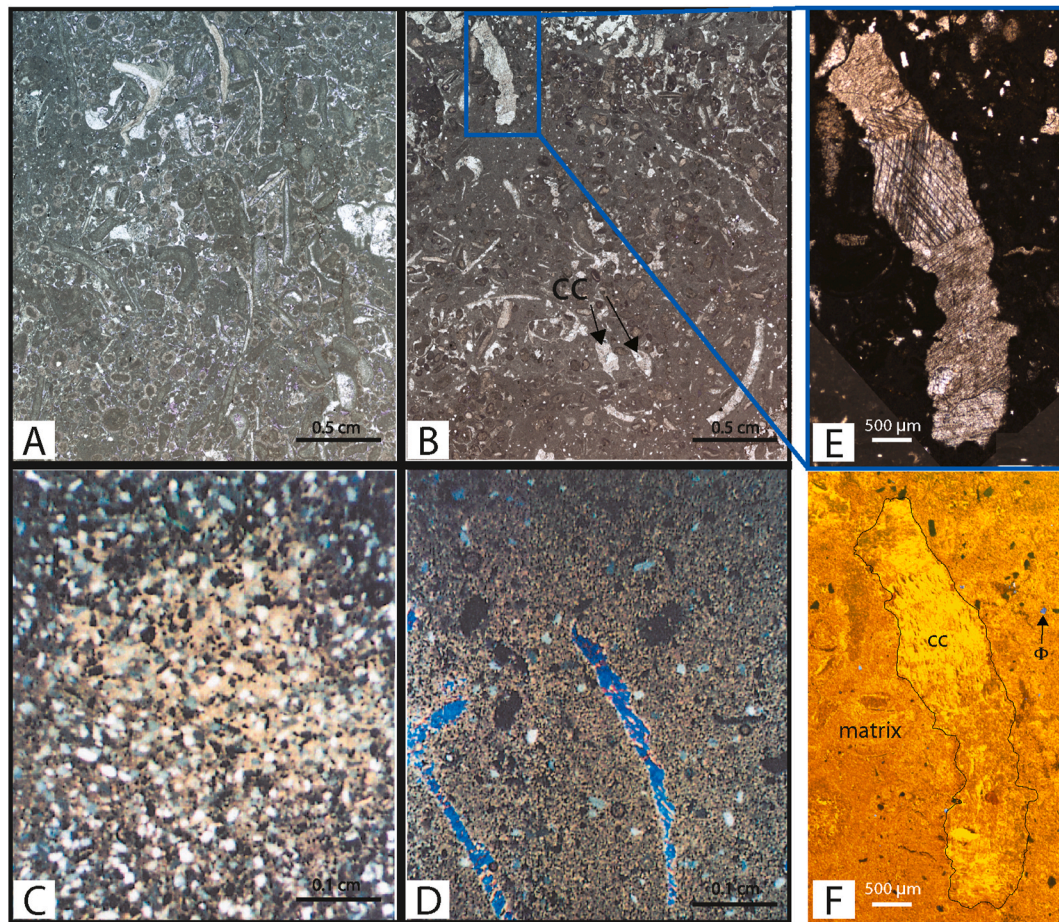


Fig. 7. Photographs in natural light of the representative facies in the drill core. A. Oolitic-bioclastic limestone. B. Gravelly bioclastic limestone. C. Fine sandstone. D. Silty-bioclastic dolomite. E. Close-up of a fossil-filled with a calcite cement in natural light and F. under cathodoluminescence.

meter with local stylolite clusters located at 3294.29 m, 3326 m, 3461.05 m, and 3487.08 m (Fig. 5A). The distribution of stylolite classes along the drill core indicates a predominance of class 3 stylolites between 3245 m and 3350 m while class 2 stylolites are mainly located near 3500 m. Classes 1 and 4 (Fig. 5B) are not sufficiently represented in the dataset to study their distribution statistically.

5.5.2. Stress inversion of stylolite roughness

52 stylolites were analyzed in the oolitic and bioclastic limestone facies and processed using SRIT (Table 3). For each stylolite, the binned Fourier power spectrum was plotted against the spectral frequency k (Fig. 10), and a nonlinear regression with fixed Hurst coefficients was modeled and fitted through the maximum of points. 41 stylolite profiles out of 52 showed a good fit to the curve (Fig. 10A and B), while 11 were not in accordance with the chemo-mechanical model (Fig. 10C and D) and were discarded. The final stylolite dataset comprises 3 class 1, 11 class 2, 25 class 3, and 2 class 4 stylolites (Fig. 5B).

We randomly checked the validity of the uniaxial strain hypothesis by obtaining L_c on 82 profiles cut orthogonal to the studied stylolite track. As all results show consistent L_c values along the two cuts (within the 23% uncertainty), we further used equation (2) to compute the vertical stress magnitude with the elastic coefficients of the Sendji limestone determined from mechanical tests ($E = 25$ GPa; $\nu = 0.24$), and interfacial energy for calcite of 0.32 Jm^{-2} (Wright et al., 2001). The roughness of the 41 selected stylolites showed L_c values from 0.085 to 2.427 mm, which correspond to magnitudes of the principal vertical stress σ_1 between 65 and 15 MPa (Table 2).

Conversion of these vertical stress magnitudes into depths using equation (3) revealed that compaction-induced pressure solution along

BPS in the Sendji Fm was active at burial depths between 650 m and 2800 m under a vertical principal stress σ_1 . The population of the calculated depths is represented in Fig. 10E as a violin plot (Hintze and Nelson, 1998). This plot shows local density estimates and provides a better visualization of the depth distribution than a traditional boxplot statistical representation. The distribution analysis shows that 47% of the stylolites exhibit a maximum burial depth between 1000 and 1300 m with a median located at about 1100 m.

We further investigated whether stylolite classes may have recorded specific maximum burial depth (e.g., Beaudoin et al., 2019) (Fig. 10E). Stylolite classes are shown here as a function of maximum burial depth revealed by signal analysis and inversion. Pressure solution along class 2 stylolites was continuous from 650 m to 2800 m whereas it mainly occurred between 1000 and 2000 m depth along class 3 stylolites. Classes 1 and 4 are too poorly represented (3 and 2 samples, respectively) in the dataset to study any relationship with depth.

5.6. Stress inversion of calcite twins

Stress inversion of calcite twins was carried out from 14 samples collected between 3245.90 m and 3510.88 m. As determined from the cathodoluminescence analysis, samples show only one twinned cement so all crystals could be processed together. Calcite grains were deformed in a thin-twin strain regime: the measured twins are thin (a fraction of μm) and straight and belong to Type I twins (Burkhard, 1993), which indicates that the temperature of deformation likely never exceeded $\sim 170^\circ\text{C}$ (Ferrill et al., 2004; see discussion in Lacombe et al., 2021a).

Our samples show a nearly random spatial distribution of optical axes of grains (Fig. 11A), which is a prerequisite for the reliable

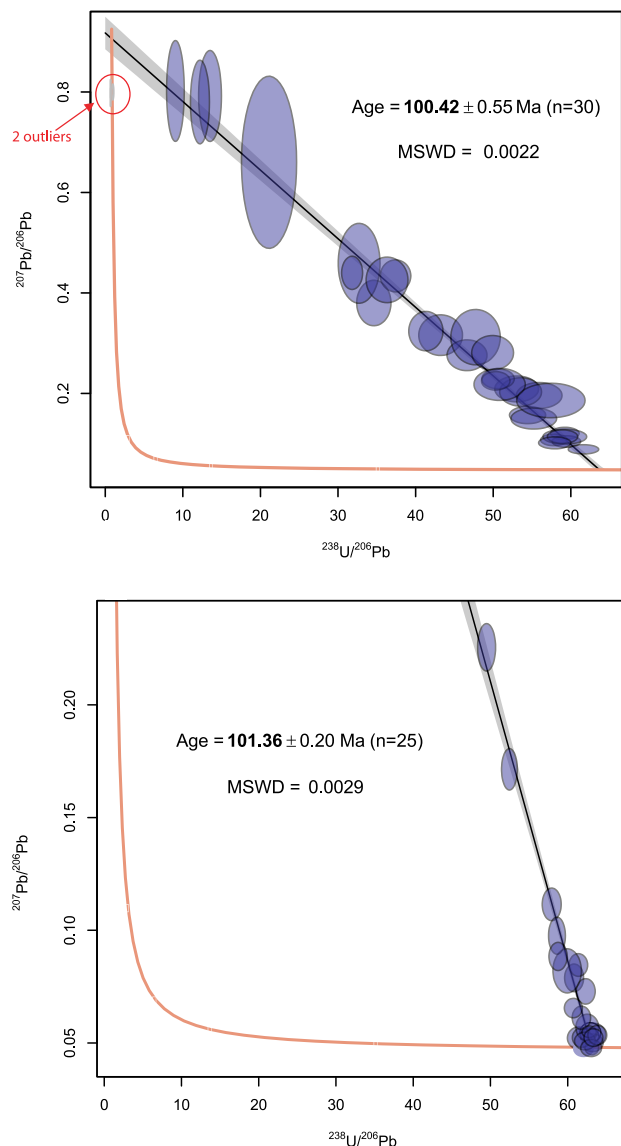


Fig. 8. Tera-Wasserburg Concordia plots showing $^{238}\text{U}/^{206}\text{Pb}$ vs. $^{207}\text{Pb}/^{206}\text{Pb}$ for calcite cement in samples 3294 (top) and 3245 (bottom) ($n = 55$). MSWD – mean square of weighted deviates.

inversion of calcite twin data for stress. Samples also highlight a modal distribution of calcite grain size ranging broadly from $>30\ \mu\text{m}$ to $<350\ \mu\text{m}$ (Table 4). Twinning strain was grossly estimated at 2%; this very small strain can be approximated by coaxial conditions so the orientation of twinning strain can be reliably correlated with paleostress orientation, which is also a prerequisite for the reliable inversion of calcite twin data for stress (Burkhard, 1993; Amrouch et al., 2010; Lacombe et al., 2021a). For each sample, this value was further considered along with the mean grain size of the size range (Fig. 11B) to define the CRSS used for the calculation of the differential stress (Table 4). Calcite twin inversion reveals that our samples are polyphase, i.e., the twin dataset results from superimposed stress tensors, each of them explaining part of the twinned planes and most of the untwinned planes. In our case, 77% of the samples yielded two or three superimposed stress tensors.

A first phase of selection was carried out to group stress tensors corresponding to similar principal stress orientations (within uncertainties) and stress regimes. Among the 26 stress tensors determined from the twinned cement of the 14 samples (see appendix), this selection revealed 7 main groups of stress tensors (Fig. 12): two extensional stress

tensor groups (A and B), two compressional stress tensor groups (C and D), and three strike-slip stress tensor groups (E, F, and G). Regarding the extensional stress regimes (vertical σ_1), tensor group A was identified in 4 samples and is characterized by a σ_3 oriented \sim N-S and by mean differential stress magnitudes of 38 MPa ($\sigma_1 - \sigma_3$) and 17 MPa ($\sigma_2 - \sigma_3$). Tensor group B was recognized from 3 samples, with a σ_3 oriented \sim N100 and mean differential stress magnitudes of 42 MPa ($\sigma_1 - \sigma_3$) and 27 MPa ($\sigma_2 - \sigma_3$) on average. Regarding the compressional stress regimes (vertical σ_3), groups C and D were identified from 6 to 3 samples, respectively. Tensor group C is characterized by a σ_1 oriented \sim N170 and mean differential stress magnitudes of 48 MPa ($\sigma_1 - \sigma_3$) and 22 MPa ($\sigma_2 - \sigma_3$). Tensor group D is characterized by a σ_1 oriented \sim N100 and mean differential stress magnitudes of 59 MPa ($\sigma_1 - \sigma_3$) and 31 MPa ($\sigma_2 - \sigma_3$). Regarding the strike-slip stress regimes (vertical σ_2), tensor groups E, F, and G were identified from 3, 5, and 2 samples, respectively, and are characterized by a σ_1 oriented N143 (E), N020 (F), and N095 (G) and by mean differential stress magnitudes of 55 MPa ($\sigma_1 - \sigma_3$) and 26 MPa ($\sigma_2 - \sigma_3$) for E, 49 MPa ($\sigma_1 - \sigma_3$) and 22 MPa ($\sigma_2 - \sigma_3$) for F and 42 MPa ($\sigma_1 - \sigma_3$) and 17 MPa ($\sigma_2 - \sigma_3$) for G. Samples associated to these tensors are spatially distributed over the entire studied core interval. No evidence of tensor grouping was observed, suggesting that these tensors are post Lower Sendji deposition.

5.7. Fracture types and distribution

70 fractures (sealed and open fractures) were identified in the drill core within the Sendji formation (Fig. 13). These fractures are distributed throughout the reservoir, with a mean linear fracture density of about 0.5 fracture/meter for the complete core (TotalEnergies internal report; this work), but one depth interval, between 3400 m and 3541 m, appears to be more particularly fractured in sequence 1. In this interval, which corresponds to a dolomitic facies both large (decametric length) and small (centimetric length) sealed fractures are present. The fractures present a range of dips and show evidence for (1) a normal shearing mode (mode II) and (2) an undetermined opening mode. Despite scattering, the distribution of fracture directions indicates the predominance of two main sets: a set comprising fractures striking NNW-SSE (N140° to N165°) and dipping \sim 50–60°W (set 1) and a set comprising fractures striking N95 and with variable dips toward the North (set 2) (Fig. 13A and B).

5.8. Burial model

The burial model generated from well and seismic data describes the burial history of all N’Kossa field formations and, in particular, the burial history of the post-rift Sendji Fm. An erosional episode occurred around 118 Ma, represented by \sim 75 m of uplift affecting pre-salt formations only. This event also marks the beginning of the post-rift phase with the deposition of the Chela Fm. Three main phases of burial of the Sendji Fm can be distinguished based on contrasting burial rates: (1) a phase of rapid burial (about 100 m/Ma) between 113 Ma and 92 Ma, coeval with deposition of the Sendji Fm and the Likouala Fm; (2) a plateau-like phase (about 8 m/Ma) ending with a slight uplift between 66 Ma and 34 Ma (3.3 m/Ma) and (3) a last phase of rapid burial from 34 Ma onward (about 50 m/Ma) coeval with deposition of the Paloukou Fm.

6. Discussion: burial, structural and paleostress history of the Sendji Fm in the N’Kossa structure and implications for the post-rift evolution of the Congolese passive margin

6.1. Timing of salt tectonics, cementation and stylolitization in the Sendji Fm

The Sendji Fm experienced salt tectonics early during its burial history, between 110 and 80 Ma, which resulted in visible structural

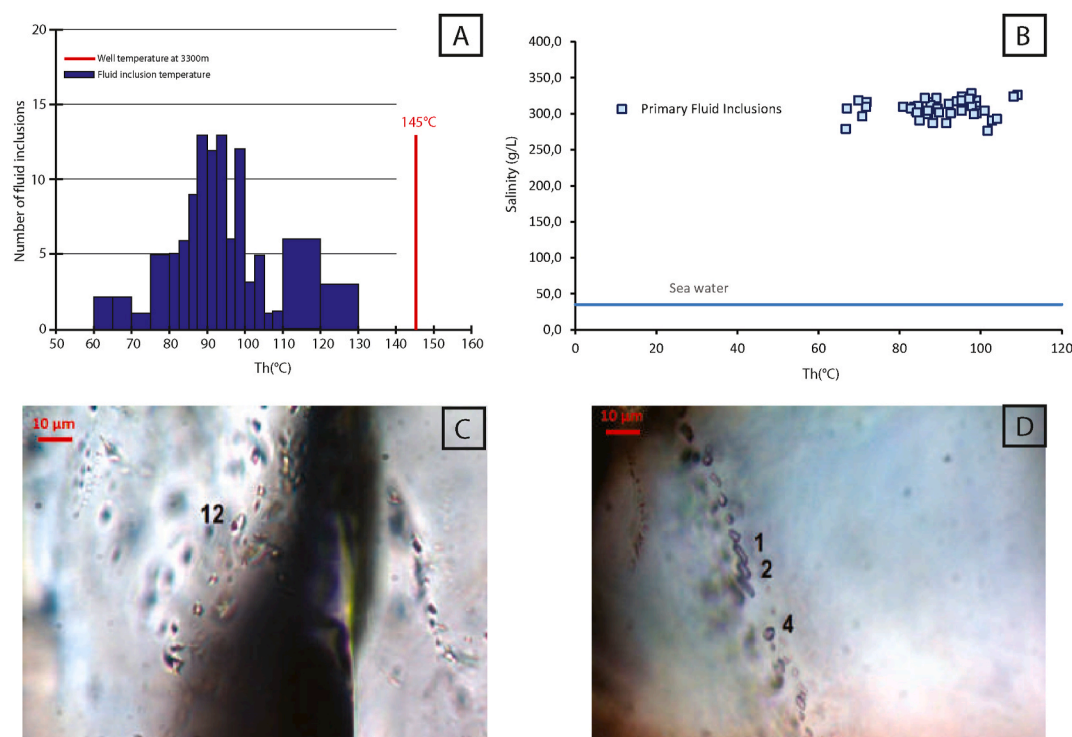


Fig. 9. A. Histogram of homogenization temperatures and B. plot of salinity against homogenization temperature determined from fluid inclusion microthermometry. C. Photographs of primary fluid inclusions in samples 3294 (left) and 3323 (right).

Table 2

Multitriax and Brazilian test results for two representative samples of the oolitic-bioclastic limestone facies, sampled in 3491 m depth in the drill cores. Samples for multitriax were tested at 10, 30, and 50 MPa confining pressure (Pconf).

Multitriax test						Brazilian test
Pconf	yield	rupture	estimated rupture	friction angle	cohesion	tensile strength
MPa	MPa	MPa	MPa	Degree	MPa	MPa
10	40	–	47.2			
30	80	–	94.4	20.5	9.8	3.08
50	110	129.8	–			

remains as shown in Figs. 3 and 4. The structural map (Fig. 3) and the seismic section of the N'Kossa field (Fig. 4) illustrate the structural setting of Well 1 in the N'Kossa structure. Listric normal faults offsetting the post-rift formations reveal local extension and notably depict a raft structure, on top of which the Sendji Fm was sampled. The structure, laying on a thin salt pillow of Loeme Fm, is bounded by major N–S to NE–SW listric normal faults (Fig. 3). The gravity tectonics occurring mostly from Aptian to Cenomanian dismantled the first post-salt sediments into disjointed rafts, either cored by lower or upper Sendji sediments. The gravity-driven salt tectonics extended until the late Cretaceous with the Likouala Fm (Fig. 4) continuously filling the gaps between the divergent rafts. These thin-skinned tectonic processes were compensated by listric normal faults bounding rollover- or turtle-type structures. N'Kossa's fairly isopach Sendji sequences are bounded by listric faults and segmented by normal NW–SE to NE–SW faults (Figs. 3 and 4). Their activity is mostly Cenomanian, during the deposition of the Likouala Fm, with tens to hundreds of meters of vertical throw. Some of the bounding faults are interpreted to have had a continuous activity until Paleogene with a very low displacement of the Madingo Fm, mostly linked to sedimentary loading or differential compaction of the carbonaceous rafts vs the clayey inter-raft Likouala filling. The major western bounding normal fault remained active until recent times, with very low

displacement reflecting likely late local accommodation within the sedimentary sequence rather than continuing salt-related extensional tectonics.

These major normal faults rooting within the Loeme salt Fm are roughly oriented N–S as indicated in Fig. 4 and therefore reflect roughly E–W oriented thin-skinned extensional deformation in the upslope domain of the margin. This extension is likely to be related to the gravitational movements of the salt of the Loeme Fm which progressively flowed downslope westward in response to sedimentary loading and accumulated several tens km further west, in the margin compressional domain. The structural style of the deformation of the post-rift sequences was therefore dominated by thin-skinned extensional tectonics (Wonham et al., 2010), mainly during the late Cretaceous. The structure of N'Kossa, therefore, recorded mostly a late Albian to Cenomanian gravity-driven extensional salt tectonics, followed by some sedimentary-driven slight gravity sliding effects rather localized to the main western bounding faults.

During the phase of salt tectonics, the Sendji Fm was progressively buried and underwent diagenesis marked by precipitation of the main calcite cement. U–Pb geochronology reveals an age of around 101 ± 1 Ma for this cement, pointing towards early cementation soon after the deposition of the Lower Sendji (between 112 and 104 Ma), during the deposition of the Upper Sendji (from ~104 to 99.6 Ma). Fluid inclusions microthermometry shows that this cement precipitated from a fluid with 10 times the salinity of seawater. This extremely high salinity could relate this fluid to the brines associated with the Loeme salt layer beneath, which was undergoing gravity-driven flow at that time. Yet the high temperature of precipitation ($Th = 90^\circ\text{C}$) is not compatible with the burial depth at which the studied strata were expected to be (950 m) at the time of precipitation (101 Ma), even considering the rather high geothermal gradient of $44^\circ/\text{km}$ (TotalEnergies internal report). Thus, one can consider the contribution of high-temperature fluids of deep origin in the basin, possibly from the basement, and a rapid fluid ascent through the salt layer thanks to the normal faults related to the early salt tectonics. Note however that constraining the origin and migration

Table 3

Results of stylolite roughness inversion technique. σ_V is calculated with a value of $E = 25$ GPa and $\nu = 0.24$. Rounded up with an uncertainty of 12%.

Stylolite characteristics (n = 41)											
Sample	Class	Insoluble Thickness (mm)	Crossover Length (mm)	σ_V (MPa)	Depth (m)	Sample	Class	Insoluble Thickness (mm)	Crossover Length (mm)	σ_V (MPa)	Depth (m)
3294.27_1	1	0.330	2.04	16	691	3245.75_6	3	0.06	0.607	30	1250
3294.27_3	3	0.047	0.56	31	1300	3245.75_5	3	0.113	0.393	37	1600
3294.27_4	3	0.044	0.26	44	1900	3294.14_3	3	0.1	1.077	22	950
3294.27_5	3	0.048	0.91	24	1050	3326.38_4	3	0.07	0.264	45	1900
3326.38_1	3	0.64	0.18	55	2300	3326.53_1	2	0.41	0.369	38	1600
3326.38_3	4	0.955	0.96	24	1000	3326.53_2	3	0.1	0.786	26	1100
3326.38_5	3	0.098	0.831	25	1080	3464.30_1	3	0.7	0.558	31	1300
3326.38_6	3	0.118	0.334	40	1700	3487.30_1	3	0.4	0.255	46	1950
3294.14_1	3	0.58	0.378	38	1600	3294.27_5	3	0.048	0.91	24	1050
3294.14_2	3	0.1	0.923	24	1000	3487.60_0	1	0.06	1.057	23	1000
3294.14_4	3	0.052	0.836	25	1100	3487.60_1	1	0.4	0.47	34	1450
3294.14_5	3	0.04	0.769	27	1150	3488.79_1	3	0.3	0.203	51	2150
3294.14_6	3	0.05	0.685	28	1200	3491.48_0	2	0.2	2.427	15	650
3294.14_7	4	0.19	0.896	25	1050	3491.88_1	2	0.48	1.026	23	1000
3245.75_1	2	0.5	0.331	40	1700	3491.88_2	2	0.48	0.927	24	1000
3294.43_1	3	0.99	0.392	37	1600	3492.27_1	2	0.21	0.127	65	2800
3326.27_1	3	0.176	1.069	53	955	3492.27_2	2	0.162	0.25	47	1970
3461.05_1	2	0.378	0.843	25	1050	3488.75_1	2	0.22	1.34	20	853
3245.75_2	3	0.05	0.399	37	1550	3487.60_2	2	0.28	0.209	51	2150
3245.75_4	3	0.07	0.331	40	1700	3461.05_4	2	0.085	0.085	55	2320
3245.75_7	3	0.029	0.954	24	1000						

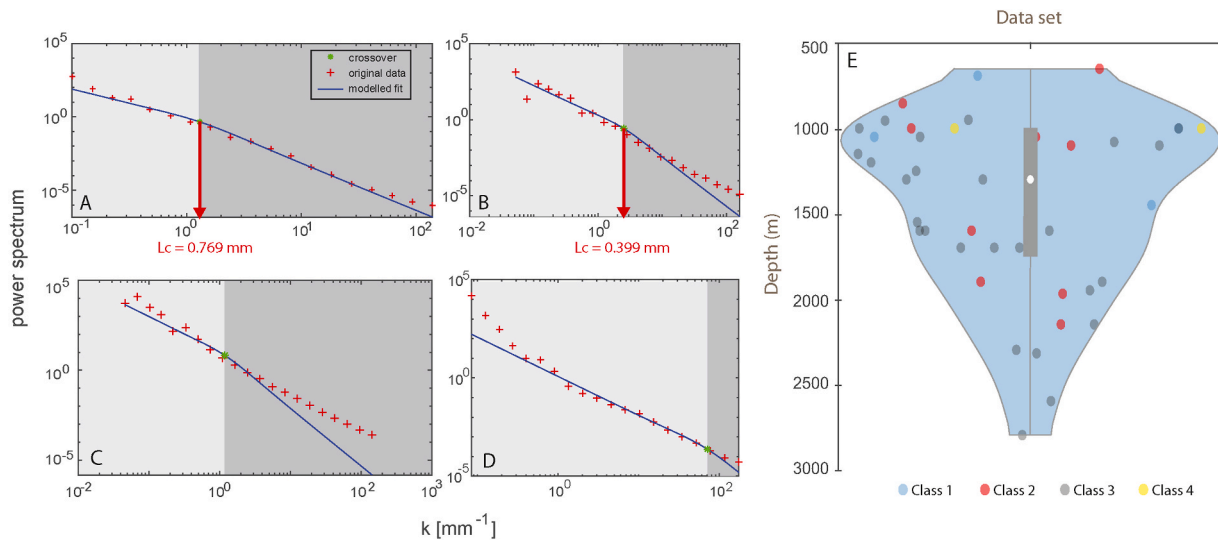


Fig. 10. Examples of Fourier power spectrum log-log plots. A. Successful inversion result for sample 3294.14_5 which is associated with a crossover length (L_c) of 0.769 mm. B. Successful inversion result for sample 3245.75_2 with an L_c of 0.399 mm. C, D. Failed inversion result where stylolite roughness inversion is missing large-scale data (C) and small-scale data (D). E. Violin plot of stylolite inversion results showing the heterogeneity of the depth distribution calculated from L_c values. The vertical bar represents the distribution of the data between the minimum and maximum values (at the extremities of the bar), the grey box plot displays the first quartile (at the top) and third quartile (at the bottom) whereas the white point displays the median.

pathways of the cementing fluids would require more geochemical proxies (e.g. Beaudoin et al., 2022), which is beyond the scope of this study.

The depth ranges of active stylolitization revealed by the inversion of the roughness of BPS projected onto the burial model indicate that the most superficial stylolite stopped its activity at 102 Ma (within uncertainties) (Fig. 14), so during the cementation. We can reasonably conclude that the (beginning of the) stylolitization was coeval with the (dated) cementation. From this point, the pressure-solution related to compaction continued at the first order until 15 Ma. In more detail however, 85% of the BPS ceased their development between 102 and 75 Ma (650–2000 m), and most of them between 1000 and 1600 m, as shown in Fig. 10. Only 15% of the studied population was still active at higher depths (between 2200 and 2800 m \pm 12%). This bimodal

distribution can be interpreted as a two-phase history of pressure solution, with a high activity below 1600 m of burial, and a lower activity between 2200 and 2800 m of burial. Interestingly, the period of time when burial stopped and the reservoir even uplifted (70–33 Ma, Fig. 14) corresponds to the depth range at which only a few stylolites halted (or none, if considering the uncertainty on each stylolite, Fig. 10). After 15 Ma, no BPS seems to have developed. The first phase of very active pressure-solution was also documented in the underlying pre-rift and pre-salt Toca Fm (Bah et al., 2023), and it coincides with the first burial phase characterized by the greatest burial rate (Fig. 14). That could suggest a potential correlation between the burial rate and the end of dissolution by stylolitization of the Sendji Fm, that we propose to relate to a higher saturation rate during the fast burial and associated sedimentary load increase. Our dataset does not allow us to discuss whether

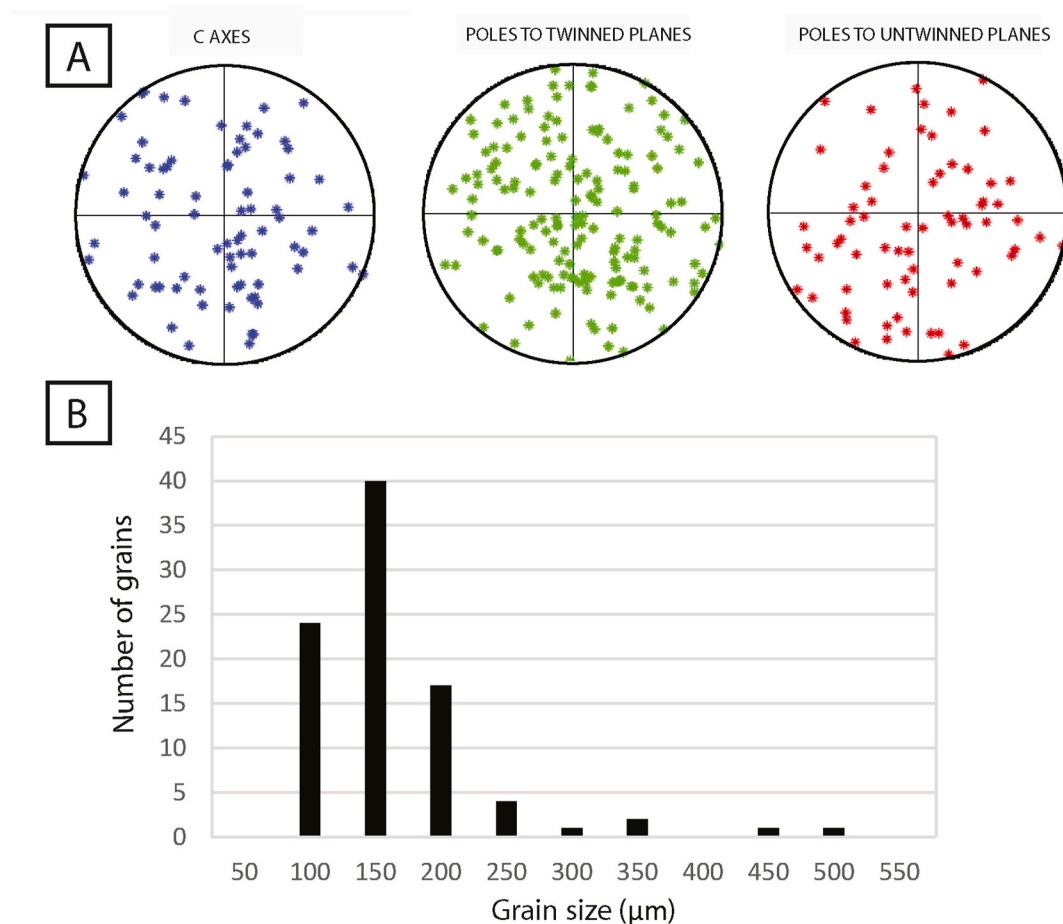


Fig. 11. A. Example of the spatial distribution of optical axes (blue) and poles to twinned (green) and untwinned (red) planes for a sample studied using CSIT-2 (sample 3454.69). B. Example of grain size distribution in the same sample.

all stylolites started their development at the same time and halted at variable depths for different local-scale reasons (sensu Beaudoin et al., 2019, e.g., local high fluid pressure, saturation of the dissolution plane, clogging of the surrounding porosity), or if stylolites that halted deeper started their development later during burial history (sensu Ebner et al., 2010). Also, we can discuss neither the impact of the sedimentary texture nor of the stylolite morphology on these inverted depths.

6.2. Timing and significance of successive paleostress regimes

The stress orientations discussed in this section are described in the present-day position of Africa.

6.2.1. Timing of the reconstructed paleostress regimes

In order to establish the timing of the paleostress regimes revealed by calcite twinning, we adopted the following workflow (Fig. 15A). The Sendji deposition age together with the absolute age of the calcite cement yield time constraints at the very beginning of the story, i.e., early fluid circulation and cementation. The distribution of depth ranges of activity of BPS as revealed by SRIT projected onto the time-burial evolution curve for the Sendji Fm (Fig. 15B) defines the time periods of compaction-related pressure-solution, hence the periods dominated by a stress regime with a vertical σ_1 . Given the previously-advocated observation that BPS develops until σ_1 is no longer vertical, one can derive the time at which σ_1 switched from vertical to horizontal in response to the tectonic stress becoming high enough to overcome the burial stress (Beaudoin et al., 2019, 2020a; Labeur et al., 2021; Lacombe et al., 2021b). This constrains the time periods when the strike-slip and compressional stress regimes (horizontal σ_1) recorded by calcite twins

prevailed (Fig. 15B). These time constraints combined with published paleostress reconstructions in onshore western and southern Africa enable to depict a consistent scenario of the stress evolution during the burial history of the Sendji Fm.

The period of stylolitization between ~102 and 75 Ma was likely dominated by a stress regime with vertical σ_1 (Fig. 14). It is therefore likely that the extensional stress tensors groups (A and B) recorded by calcite twinning prevailed within this time interval. Stress tensor groups E, C and F associated with σ_1 trending NNW-SSE to NNE-SSW, recognized at other localities (Viola et al., 2012; Nkodia et al., 2020), hence of regional significance, can be assigned to the “End Cretaceous event” ~67–60 Ma (Guiraud and Bosworth, 1997), on the basis of consistent compressional trends. This timing fits with the onset of the 70–33 Ma time interval when burial stopped, the Sendji reservoir uplifted and few or no BPS were active (Fig. 14). Finally, because the current state of stress is dominated by ~ E–W compression (Heidbach et al., 2016), and because after ~15 Ma no BPS seems to have developed, which supports that σ_1 has definitely switched from vertical to horizontal since then, we propose that the stress tensor groups G and D prevailed since ~15 Ma (15–10 Ma to be conservative taking into account uncertainties) onwards.

6.2.2. Significance of the reconstructed paleostress regimes

6.2.2.1. Local extensional stresses related to salt tectonics in the N’Kossa field. Based on the location of the well from which the Sendji Fm was cored, the NNW-SSE striking, west-dipping fractures which display small extensional jogs filled with anhydrite (set 1 in Fig. 13A) are likely

Table 4
Paleostress tensors determined from calcite twin inversion (CSIT-2) for each sample (from −3510.88 m to −3245.90 m). The quality of each tensor is estimated based on several criteria such as the stability of principal stress orientations, the value of the penalization function and the number of incompatible untwinned planes (A: very good quality, B: good quality and C: poor quality).

Depth (m)	Number of grains	Crystal size range (μm)	Total number of TP/UP	Number of compatible TP/UP	Tensors	σ1 trend-plunge(°)	σ2 trend-plunge(°)	σ3 trend-plunge(°)	Φ	Penalization Function	τ_s^{min}	% of explained twin planes	CRSS (MPa)	(σ1–σ3) MPa	(σ2–σ3) MPa	Quality
−3245.90	66	50–450	106/67	34/56	1	N011-68	N080-08	N167-20	0.51	0.46	0.213	32	9	43	22	B
−3292.33	79	30–100	153/84	34/56	2	N017-11	N097-40	N120-48	0.53	0.87	0.183	32	9	49	26	B
				61/64	1	N135-34	N150-55	N50-07	0.6	1.7	0.146	40	12	80	48	C
−3294.35	76	100–500	178/50	52/70	2	N95-37	N04-01	N93-53	0.48	0.87	0.145	34	10	67	40	B
													12	80	40	
				64/42	2	N099-14	N002-28	N033-59	0.55	0.95	0.09	42	10	67	33	A
													7	78	43	
−3323.52	51	100–500	118/32	44/27	1	N001-70	N91-00	N001-20	0.25	0.25	0.2	38	8	89	49	B
													7	43	18	
				44/24	2	N019-16	N177-73	N108-06	0.43	0.66	0.16	36	8	50	22	A
													7	35	19	
−3326.62	58	100–300	102/54	40/47	1	N001-70	N91-00	N001-20	0.25	0.25	0.2	38	8	40	22	B
													7	67	26	
	76	100–450	170/82	51/70	1	N016-11	N040-77	N107-05	0.39	0.93	0.09	38	8	76	30	A
													10	50	28	
−3454.69	76	100–450	170/82	40/47	2	N119-14	N85-74	N27-09	0.25	0.56	0.2	36	10	63	20	B
													10	63	20	
	76	100–450	170/82	51/70	1	N165-24	N61-30	N107-50	0.32	0.37	0.16	40	8	50	26	B
													9	56	20	
−3461.20	67	50–250	134/61	48/45	1	N176-04	N082-46	N089-43	0.53	0.90	0.16	32	12	75	29	B
													7	44	17	
	76	50–350	138/90	38/74	1	N160-17	N100-58	N61-26	0.39	1.2	0.15	36	12	60	28	B
													7	35	16	
−3461.76	76	50–350	138/90	38/74	1	N70-55	N171-08	N86-34	0.46	1.07	0.12	30	12	57	31	C
													7	33	18	
	80	100–250	175/65	52/58	1	N149-34	N081-28	N020-43	0.54	1.2	0.21	28	12	39	11	B
													10	56	8	
−3469.10	81	50–200	189/54	64/42	1	N051-58	N118-14	N020-28	0.20	0.97	0.18	30	12	76	53	A
													8	53	36	
	81	50–200	189/54	71/38	2	N012-48	N042-38	N120-15	0.70	0.66	0.16	34	12	88	48	A
													8	58	32	
−3487.19	62	100–350	146/43	55/33	1	N008-02	N008-79	N008-79	0.55	0.94	0.14	38	10	67	36	B
													6	40	21	
	72	100–300	172/44	51/36	1	N024-49	N026-41	N115-01	0.53	0.88	0.15	38	10	59	18	A
													6	35	11	
−3491.05	72	100–300	172/44	61/31	2	N006-25	N092-08	N167-63	0.31	0.87	0.17	36	10	54	28	A
													6	32	17	
	72	100–300	172/44	65/37	3	N71-05	N159-17	N178-72	0.52	0.39	0.19	30	10	68	44	A
													6	41	27	
−3510.88	83	100–350	198/51	75/44	1	N137-75	N003-11	N091-11	0.65	0.90	0.15	36	10	83	27	A
													6	50	16	
	83	100–350	198/51	75/44	1	N169-22	N077-06	N151-67	0.33	0.73	0.12	38	10	67	27	A
													6	40	16	
−3510.88	83	100–350	198/51	63/39	2	N144-51	N087-24	N191-29	0.40	0.55	0.15	38	10	59	25	B
													6	35	17	
	83	100–350	198/51	79/39	3	N028-40	N170-43	N100-20	0.50	0.93	0.17	32	10	91	46	C
													6	55	28	

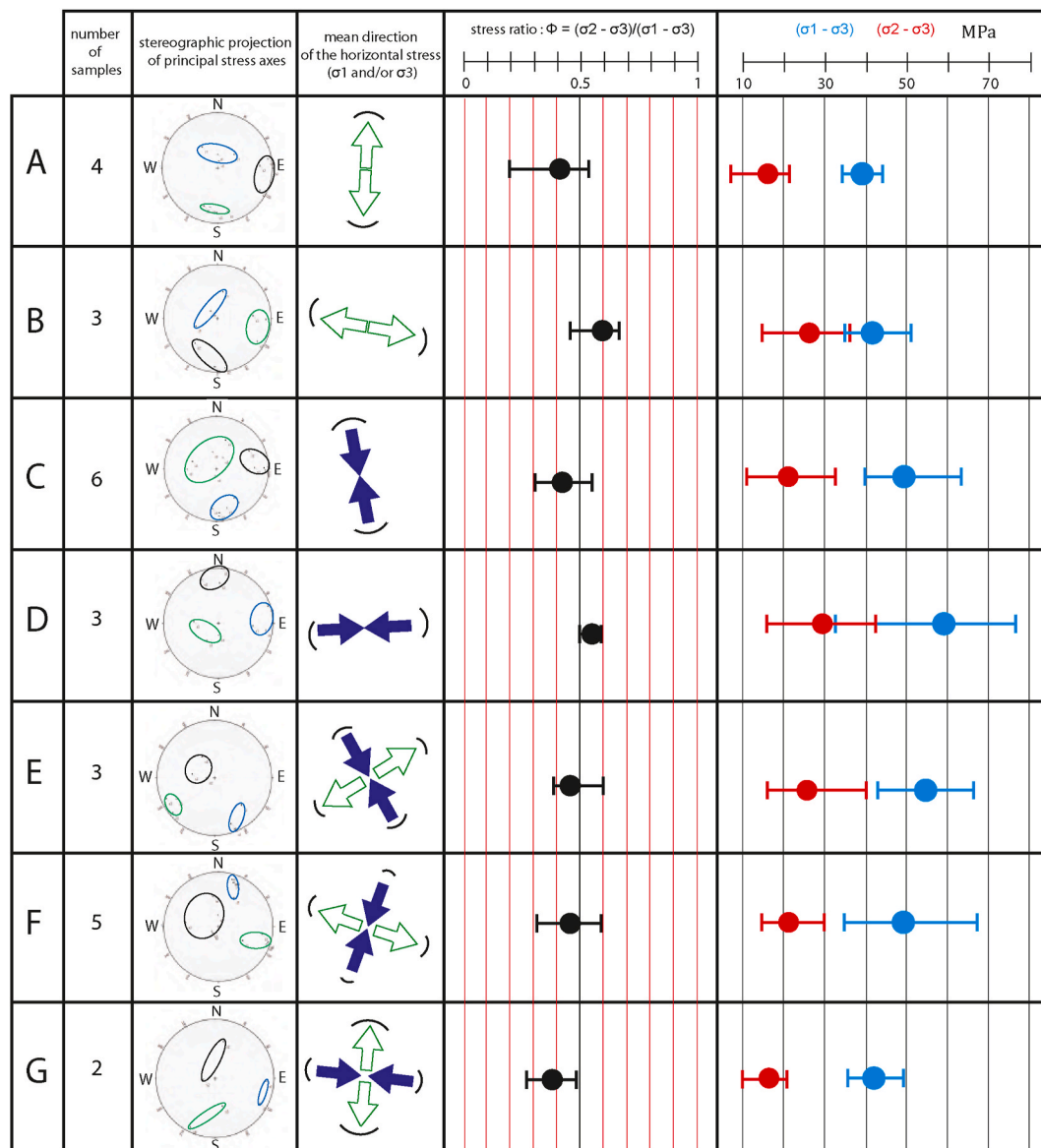


Fig. 12. Overview of stress tensor groups resulting from calcite twin inversion using CSIT-2. Each tensor group (from A to G) is characterized by a plot data in stereographic equal-area projection showing the mean orientation of the principal stress axes (blue for σ_1 , black for σ_2 , and green for σ_3) and the representation of the average orientation of the horizontal stresses as arrows (with σ_1 in blue and σ_3 in green) in map view. Each tensor group is associated with several samples from which the related stress tensors were identified. The average values of the differential stress magnitudes for each group are shown in blue ($\sigma_1 - \sigma_3$) and in red ($\sigma_2 - \sigma_3$) and the average value of the stress ratio Φ in black.

related to the large halokinetic N160° listric normal faults (Fig. 3), possibly having been even sampled within the damage zones of the normal fault network. In this hypothesis, these fractures were formed in a nearly E-W-oriented extensional regime associated with salt-related gravity tectonics in a roughly E-W direction. The extensional stress tensor group B recorded by calcite twins is therefore consistent with the formation of these mesoscale fractures and the kinematics of the listric normal fault, the vertical attitude of the σ_1 axis being also consistent with the BPS development at that time. The stress tensor group A corresponds to the second purely extensional stress regime with σ_3 oriented N-S in the present-day projected direction. Considering the complex pattern of interconnected normal faults as shown in Fig. 4 and the dome-like raft structure, it is likely that local extension may have temporarily switched or oscillated from E-W to N-S oriented extension during the paroxysm of the salt tectonics. This N-S extension is roughly consistent with the minor set (set 2) of mode II fractures as well as with the location of the well close to the northern boundary of the N'Kossa raft with a

roughly NE-SW to E-W free edge. We therefore tentatively relate the N-S extension also to the gravity-related thin-skinned salt tectonics. The two extensional stress regimes therefore would be of local significance and restricted to the detached supra-salt cover, and associated with salt tectonics from 110 to 80 Ma, without reflecting any large-scale extensional crustal strain at that time.

6.2.2.2. Far-field stresses transferred to the Atlantic margin from distant plate boundaries. During the post-rift phase, several compressional or strike-slip states of stress (horizontal σ_1) have been recorded onshore in central, western, and southern Africa (Fig. 16).

We interpret the strike-slip and compressional stress with σ_1 oriented NW-SE for tensor group E, NNW-SSE for tensor group C, and NNE-SSW for tensor group F revealed by calcite twinning as reflecting intraplate compressional stresses transferred from the distant Africa-Eurasia plate boundary. The Santonian compressional phase (85-83 Ma) described by Guiraud and Bosworth (1997) was seemingly not

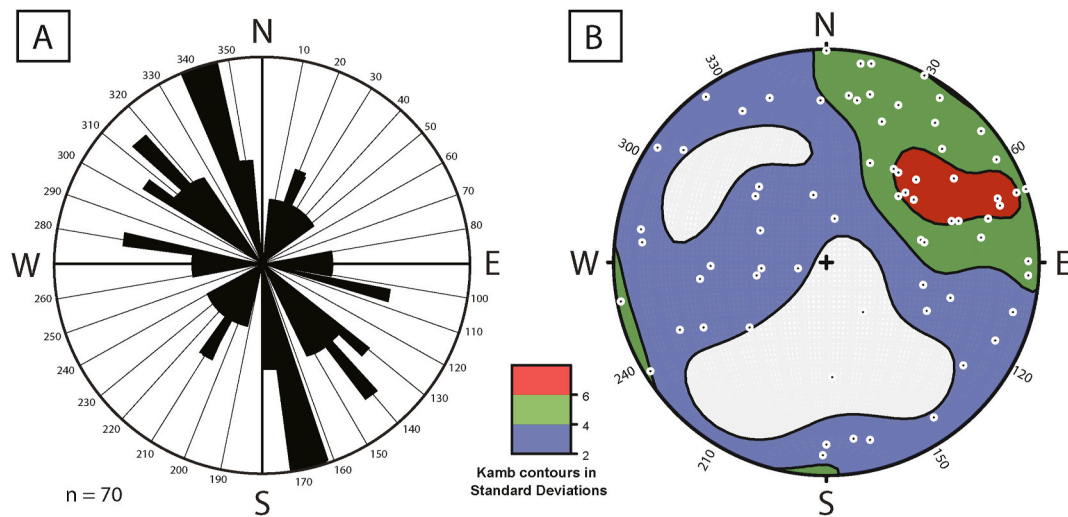


Fig. 13. A. Rose diagram of strikes for fractures described in the core sample. B. Kamb contours of fracture plane poles projected on the lower hemisphere of a Schmidt diagram.

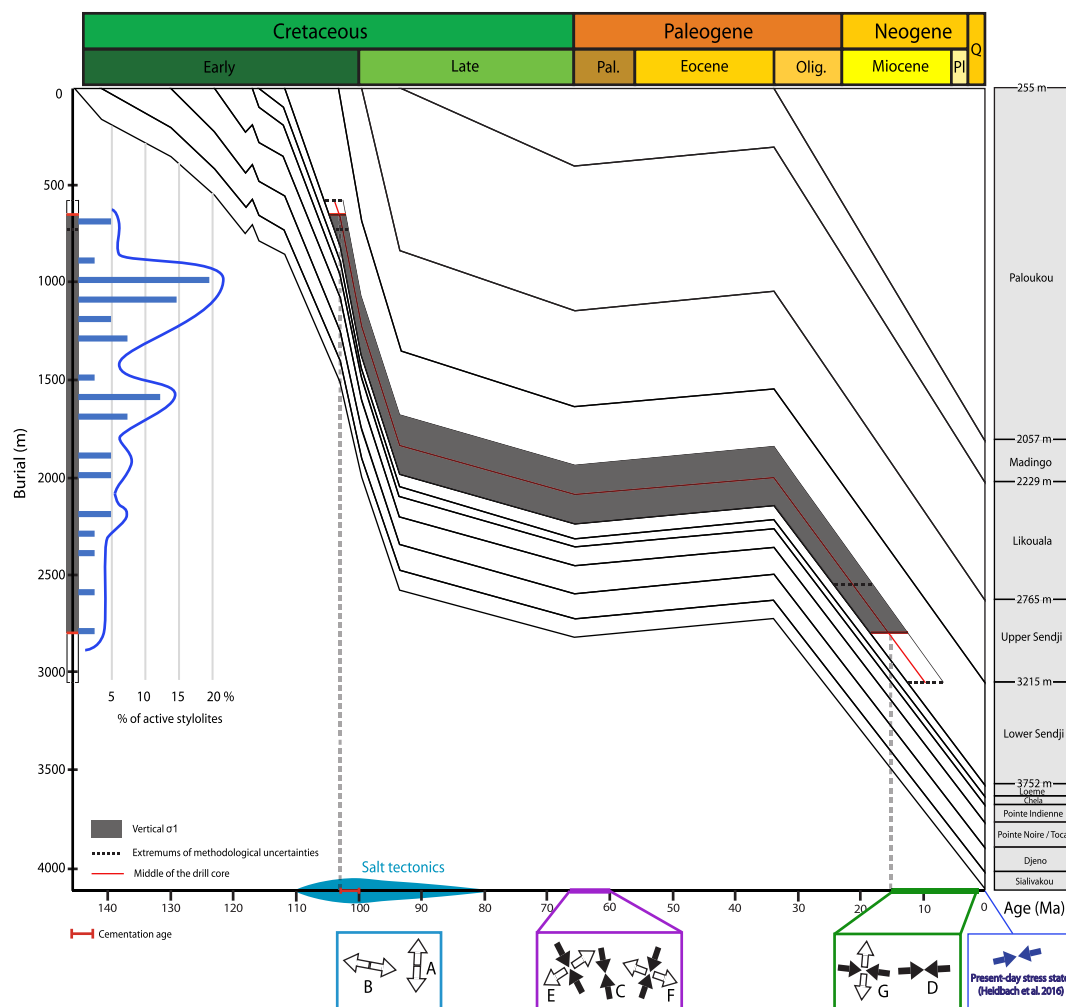


Fig. 14. Burial model of the syn-rift and post-rift formations of the Lower Congo Basin. The results of sedimentary stylolite roughness inversion in terms of depths of active pressure solution results are plotted as a depth histogram. Transitions from vertical to horizontal σ_1 periods are illustrated by grey dashed lines (at 101 Ma, 75 Ma, 30 Ma, and 15 Ma) and these estimates are based on the middle of the drill core (indicated by the red line along the burial model). Dark grey areas show periods with vertical σ_1 whereas black dashed lines indicate methodological uncertainty limits. The blue area represents the period of active salt tectonics. The average orientation of the horizontal stresses are shown as arrows (with σ_1 in black and σ_3 in white) in the map view for stress tensors likely coeval with salt tectonics (A and B, blue) possibly related to the intraplate NNW to NNE compressional event during the Maastrichtian-Paleocene times (C, E, and F, purple) and possibly related to the Atlantic ridge push (D and G, green). The present-day stress state is displayed by blue arrows (Heidbach et al., 2016).

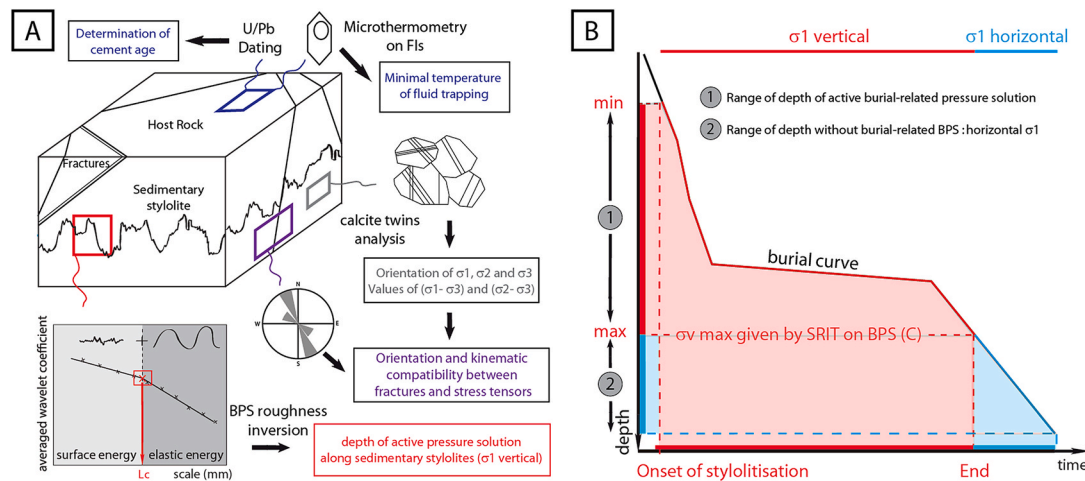


Fig. 15. A. Workflow of the multi-technique approach used in this study. B. Representation of the time conversion method for paleoburial obtained by stylolite roughness inversion using the burial model. Red periods are dominated by a vertical σ_1 as deduced from continuous stylolitization and blue periods are dominated by a σ_1 that is likely no longer vertical, hence likely horizontal.

recorded in the N’Kossa field since this period corresponds to active pressure–solution along BPS under a vertical σ_1 in the Sendji Fm (Fig. 16) and to the maximum of salt tectonic activity. The late Maastrichtian-early Paleocene N–S to NW–SE compressional episode described by Guiraud and Bosworth (1997) between 67 and 60 Ma could instead be consistent with our tensor groups C, E and F. A stress regime very close to our tensor group C was also recorded in two other locations in the pre-salt Toca Fm: (1) in a well located 2 km away from well 1 and (2) in a well located 46 km NE from well 1, closer to the continent (Bah et al., 2022). The record of this stress regime in a pre-salt formation precludes any possible halokinetic origin for this stress and therefore argues in favor of the far-field transfer of compressional crustal stresses. This supports the idea that the supra-salt formations which also recorded this state of stress were mechanically recoupled/welded to the underlying formations at that time, possibly because of the nearly complete salt removal.

The E–W compression tensor of group D is comparable to the current stress regime outlined by Heidbach et al. (2016). Additionally, Ziegler et al. (1995) and Guiraud et al. (2005) observed an E–W compressional stress regime in Africa, while Delvaux and Barth (2010) and Nkodia et al. (2020) noted a similar trend in the Congolese margin and continental Congo. These findings suggest a possible common origin for this compression. Ziegler et al. (1995) and Nkodia et al. (2020) further proposed that this intraplate E–W compression that prevailed from the Miocene onwards likely reflects a ridge push effect. The prevalence of this stress field with horizontal σ_1 since ~15 Ma in the N’Kossa field would coincide with the definite end of compaction-related stylolitization there and may reflect the final switch of σ_1 from vertical to horizontal due to gravitational ridge push forces overcoming overburden weight. Similarly, the strike-slip stress regime with σ_1 oriented E–W (tensor group G) marks the onset of the ridge push effect during the Miocene, evolving towards pure compression in the present-day. This

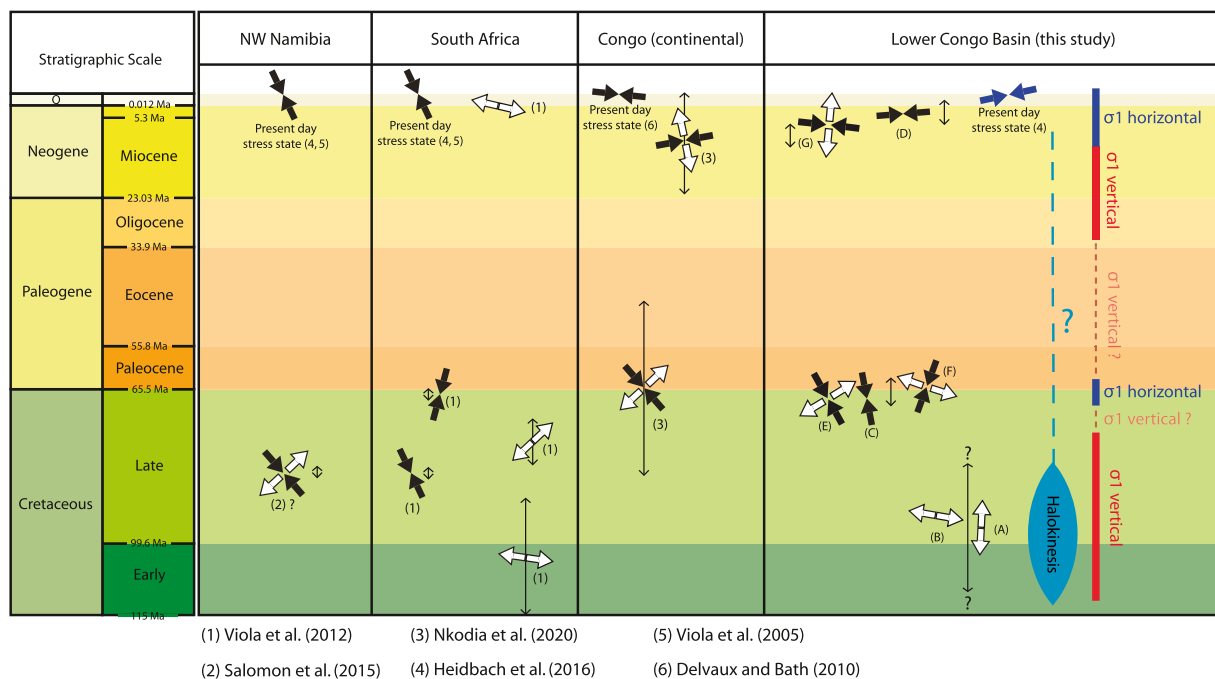


Fig. 16. Compilation of time distribution of tectonic events and related stress orientations (projected to the present-day position of Africa) since early Cretaceous time recorded in Congo, North West Namibia, and South Africa, together with the results of the present study.

interpretation is consistent with the suggestion by Wiens and Stein (1983, 1985) that the ridge push effect can efficiently control lithospheric stress long after the initiation of the spreading ridge.

The contribution of the ridge push effect to the Miocene to the present-day stress field can theoretically be questioned because of the large distance between the oceanic ridge and the passive margin (about 2400 km) since 15 Ma. However, the magnitude of the ridge-push force appears to be significantly less than the integrated strength of the oceanic part of the African (Nubian) plate, so the oceanic part of the plate is very little deformed and the stresses associated with the gravitational potential energy of the mid-Atlantic ridge may be transferred far into the interior of the oceanic and continental parts of the African plate (Mahatsente and Coblenz, 2015). Our interpretation is also in line with the work of Withjack et al. (1995) who reported that during the development of the passive margin of southeastern Canada, the Fundy rift basin on the western edge of the margin experienced shortening possibly associated with sea-floor spreading processes such as ridge push or continental resistance to plate motion. Recently, Nkodia et al. (2020) proposed that the present-day stress pattern in West-central Africa could be related to stress loading of the passive margin and interior Congo by the oceanic transform faults extending onland, triggering the reactivation of well oriented fault systems on the continental margin and onshore. In this scenario, the present-day stress pattern would not be controlled strictly speaking by the ridge push itself but would still be linked to a seafloor spreading process.

One can nevertheless wonder about possible alternate deep stress sources for the Miocene to present-day E-W compression. Medvedev (2016) suggest a mixed origin of the state of stress throughout the African plate, including density variations within the lithosphere, traction of the basal mantle, and flexural loading of the lithosphere in addition to the ridge push effect, in agreement with the findings of Pascal and Cloetingh (2009) in the south Norway shelf. The respective contributions of these various stress sources to the Miocene to present-day stress field at the west Africa passive margin remain to date poorly constrained.

To sum up, the inversion of calcite twins applied to the Sendji Fm suggests that the west African passive margin experienced a complex post-rift tectonic history including compressional events possibly related to far-field tectonic and gravitational stress transfer from active plate boundaries. Our interpretations are therefore consistent with earlier claims that the late Cretaceous–Cenozoic intraplate contractional deformation at the Norwegian continental shelf (northern Atlantic) was possibly related to far-field effects of active plate-margin processes and transfer of stresses across the plate as a consequence of the Alpine orogeny, with additional significant contribution of ridge push from the North Atlantic spreading particularly during the Neogene (Våagnes et al., 1998).

6.3. Stress magnitudes in the Sendji Fm and implications for fracture prediction in the reservoir

The combination of vertical stress estimates derived from the burial model with differential stress values provided by calcite twinning paleopiezometry enables us to estimate principal stress magnitudes at the time of deformation (Lacombe and Laurent, 1992; Lacombe, 2007). The comparison of the resulting values against the strength of the intact rock (i.e., its failure envelope) would serve not only as a test of the internal consistency of our result but may also help predict whether fracturing can be expected, hence predicted in the reservoir at the time of the successive stress regimes. To that aim, σ_V magnitudes were calculated using equation (3) considering the weight of the overlying rock column either in dry conditions, $\sigma_V = \rho gh$ assuming nearly 0 fluid pressure, or assuming hydrostatic fluid pressure, $\sigma_V = (\rho - \rho_w)gh$, with ρ the dry density of the rock column above the stylolite (g.m^{-3}), ρ_w the density of water (g.m^{-3}), g the gravitational field acceleration (m.s^{-2}), and h the depth (m). Subsequently, we consider that the tangency of the (σ_1 – σ_3) Mohr circle to the failure envelope is indicative of rock failure.

The late Maastrichtian–early Paleocene NNW to NNE compressional–strike-slip tectonic event was recorded by calcite twins (stress tensor groups E, C, and F) when the formation was buried at a nearly constant depth of 2100 m, which corresponds to a mean value of the vertical stress (σ_2 or σ_3) of ~ 49 MPa in dry conditions (Fig. 17A). The Mohr circles for stress tensor group E indicate rock failure whereas the Mohr circles for stress tensor groups C and F lie below the failure envelope (Fig. 17A) but can indicate failure if we consider the 30% of uncertainties on differential stress values. Hydrostatic conditions allow for rock failure for stress tensor group C but stress tensor groups E and F lie slightly above the Mohr envelope (Fig. 17B). This suggests that rock failure can be expected but low fluid pressure conditions in the reservoir at that time. No observed fracture could be assigned with certainty to the strike-slip stress regime (tensor groups E and F), but some may have been missed during coring or misinterpreted when related to halokinesis (see section 6.2.2.1). This result is consistent with the observations of mesoscale faulting related to this event in continental western Africa (Nkodia et al., 2020; Viola et al., 2012) although the investigated rocks were different there.

For the Neogene compressional phase with horizontal σ_1 trending E–W, the estimated vertical stress for tensor group D in dry conditions is 80 MPa at present-day, while the estimated vertical stress for tensor group G is 73 MPa at ~ 10 Ma in dry conditions (Fig. 17C). The Mohr circles for stress tensor groups D and G lie below the rupture envelope in dry conditions (Fig. 17C and D) and under hydrostatic conditions (Fig. 17D) but in the latter, considering uncertainties ($\sim 30\%$), failure would, however, be possible despite being unlikely. These observations indicate that despite relatively high differential stress magnitudes (especially for stress tensor group D), this phase would not cause significant faulting and that there was likely no fluid overpressure at that time.

For the E–W and N–S extensions that we propose to relate to halokinesis, we assume a σ_V of 49 MPa in dry conditions corresponding to the maximum burial depth of the Sendji Fm at the end of the main halokinetic deformation, at about 75 Ma. The resulting Mohr circles are tangent to the rock failure envelope thus predicting extensional faulting related to this event under a nearly null fluid pressure in the reservoir (Fig. 17E). This is consistent with the occurrence of mode II fractures in our dataset (Fig. 13) and with the extensional faulting associated with salt tectonics in the N’Kossa field.

Because the unique investigated core comes from an area where two large faults intersect and because the local salt flow might have altered the far-field stress transfer, one can wonder whether the local stress record is significant and representative of the scale of the oil field. In particular, the regional stress field might have been spatially deviated locally by the structures, with additional possible stress concentration in the fault damage zones leading to overestimated, hence anomalous, stress magnitudes. It must first be noticed that the extensional stress record (stress tensor groups A and B) is consistent with the kinematics of the normal faults bounding the area investigated, and that the associated differential stress magnitudes combined with the rock strength envelope derived from geomechanical tests consistently indicate normal faulting. After the salt tectonics phase ceased, these normal faults have had limited activity, with expectedly little or no reactivation in response to the post-rift late Cretaceous–Tertiary strike-slip and/or compressional stress fields (stress tensor groups E–C–F and G–D). As a result, one can safely assume little or no spatial local deviation of the remote stress fields. This is confirmed by the similarity of the post-rift stress orientations identified in the supra-salt Sendji Fm with (1) the stress orientations reconstructed in the infra-salt TOCA formation in a slightly distant well in the N’Kossa field (Bah et al., 2022) and (2) the results of previous stress studies (e.g., Viola et al., 2012). On the same line, the Mohr constructions provide no evidence of overestimation of the stress magnitudes for stress tensor groups E–C–F and G–D, with stress magnitudes never exceeding the rock strength in agreement with the absence of any related fractures in the core. Thus, we are confident that our stress results remain valid at the first order away from the well from which they

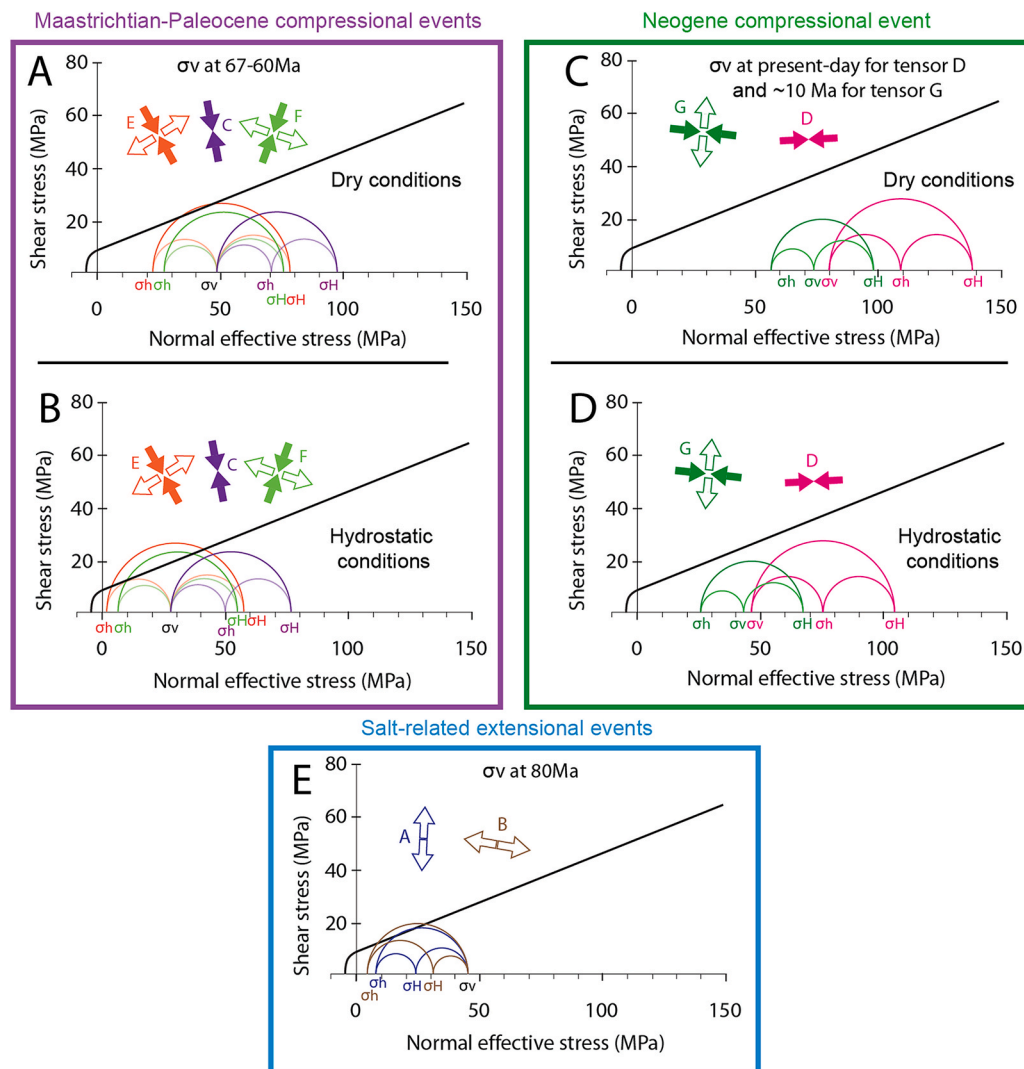


Fig. 17. Mohr diagrams showing the Mohr failure envelope of the Sendji Fm determined from rock mechanics tests and the Mohr circles related to differential stress magnitudes derived from the inversion of calcite twins from each tectonic event, in dry and hydrostatic conditions (see text for details). A, B: Mohr construction for tensor groups E, C, and F related to the far-field Maastrichtian-Paleocene compression between 67 and 60 Ma for dry conditions (A, $\sigma_V = 49$ MPa) and hydrostatic conditions (B, $\sigma_V = 29$ MPa). C, D: Mohr construction for tensor groups D and G related to Atlantic ridge push at present-day and at ~ 10 Ma respectively for dry conditions (C, $\sigma_V = 80$ MPa for tensors group D and 73 Ma for tensors group G) and hydrostatic conditions (D, $\sigma_V = 47$ MPa for tensors group D and 42 for tensors group G). E: Mohr construction for tensor groups A and B related to salt tectonics at 75 Ma in dry conditions ($\sigma_V = 49$ MPa). σ_V : vertical principal stress, σ_H : minimum horizontal principal stress and σ_H : maximum horizontal principal stress.

were established and are regionally representative.

6.4. Tentative reconstruction of the structural evolution of the N’Kossa structure

The main steps of the paleostress and paleoburial history of the Sendji Fm in the framework of the structural evolution of the N’Kossa structure are summarized through eight major stages illustrated in Fig. 18. The first stage (Fig. 18A, Early Albian) shows the deposition of the Lower Sendji on the Loeme salt, assumed to be still constant in thickness. The loading caused by the lower Sendji deposition initiated the movement of the underlying salt which began its migration toward the west of the margin. During the Upper Sendji deposition, salt turtle backs and rafts intensified deformation from the previous stage. In this context, the salt tectonics increased the flexure of the overlying sedimentary deposit and caused fractures to develop down to the salt layer. N–S faults provided pathways for hot and saline fluids to ascend at ~ 101 Ma, causing early cementation of the Sendji carbonates (Fig. 18B). During the deposition of the Likouala Fm, between 101 and 93.5 Ma, salt tectonics reached its peak activity with the development of a raft structure bounded by listric normal faults (Fig. 18C and D). At the basin scale, from 101 to 80 Ma, the maximum principal stress was vertical, associated with continuous sedimentation. In this context, the configuration of the faults that border the raft has temporarily influenced the stress field. Stress tensor groups A and B reflect the extension induced by

salt tectonics at the oil field scale. From 80 to 75 Ma, N–S and E–W extension were no longer recorded (halokinetic activity decreased significantly from 80 Ma) but σ_1 remained vertical, only burial stress being likely involved at this stage (Fig. 18D).

Fig. 18E illustrates the stress state prevailing by the Latest Cretaceous–early Paleocene (~ 67 –60 Ma). Until now, salt was abundant enough to act as a detachment level decoupling the Sendji Fm from the infra-salt formations. The progressive decrease of the salt thickness in the proximal part of the margin and its accumulation in the distal part allowed the welding of the salt detachment and the progressive recoupling of the supra-salt series with the pre-salt series and basement. As a result, the Sendji Fm recorded the late Maastrichtian–earliest Paleocene compression (stress tensor groups C, E, and F) that we interpret as being transferred from the distant Africa-Eurasia plate boundary. This far-field stress record is consistent with a cessation of sedimentation (plateau in the burial-time model) and the onset of reservoir uplift, and with a transient halt of dissolution along BPS (Fig. 15). Between 30 and 15 Ma, σ_1 became temporarily vertical again before switching definitely to horizontal from ~ 15 Ma onwards (Fig. 18F). The cessation of dissolution along BPS since ~ 15 Ma in the Sendji Fm implies that the maximum stress σ_1 was no longer vertical. Fig. 18G illustrates the record of stress tensor group G with an E–W oriented σ_1 during the Paloukou Fm deposition whereas Fig. 18H illustrates the current stress state with the complete post-rift series deposited. The Atlantic ridge push is likely to be the main distant source of this Neogene stress field.

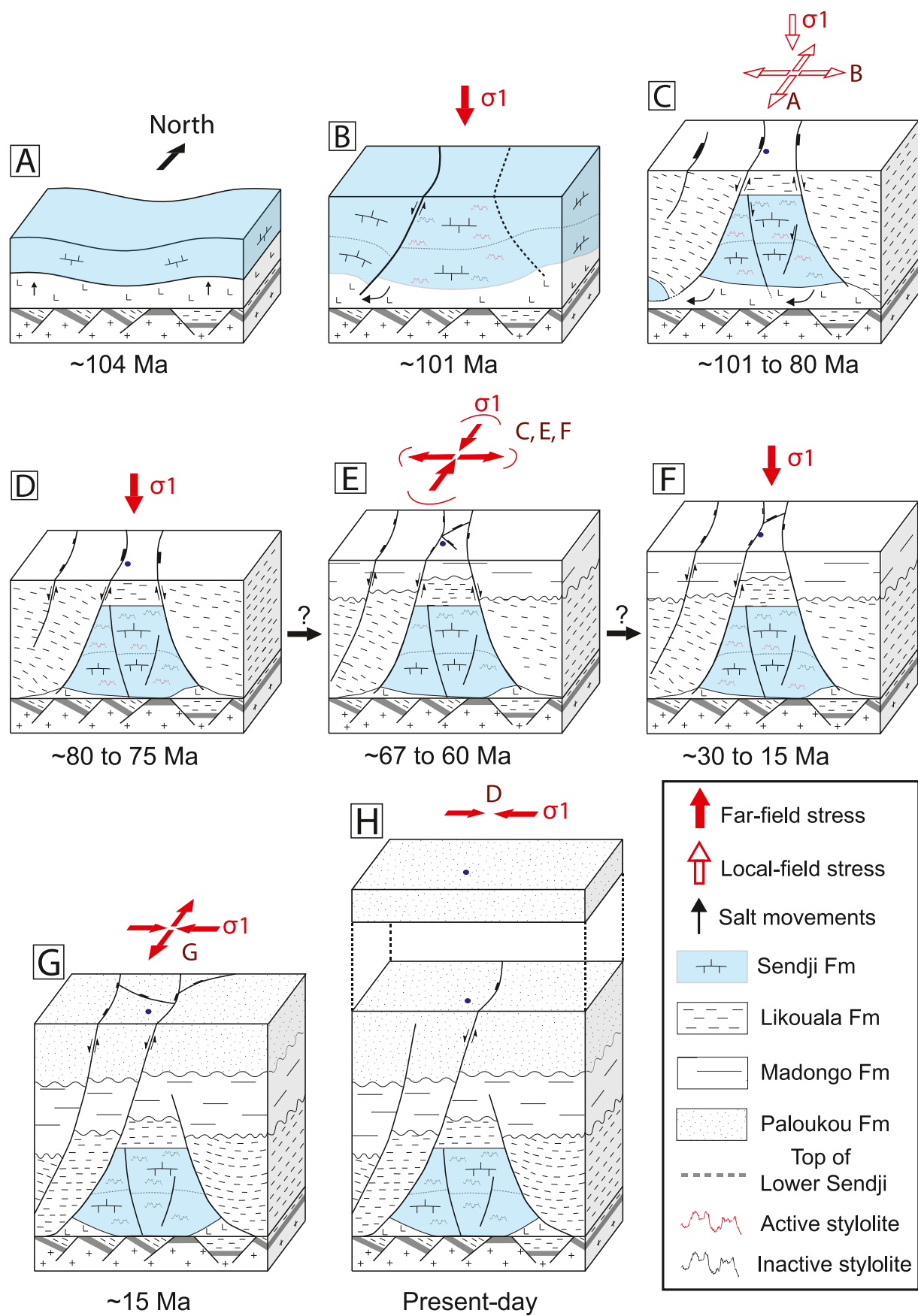


Fig. 18. Sketched structural evolution of the N'Kossa structure area and associated stress regimes at each burial stage of the Sendji Formation (blue layer), from 104 Ma to present-day.

7. Conclusions

This study focuses on the supra-salt carbonate Sendji Fm at the top of an offshore raft structure in the lower Congo basin (west Africa passive margin). The original combination of burial modeling, absolute U–Pb dating of diagenetic cement, fracture analysis, and stress inversion of calcite twins and sedimentary stylolite roughness in a 306 m drill core constitutes an original approach to obtaining unprecedented information on the burial and paleostress history of this reservoir. The analysis of calcite twins yielded successive stress regimes, the timing of which was constrained by the reconstruction of the maximum depth of active compaction-related pressure solution combined with burial modeling. During the burial, calcite twins recorded three main events: (1) extensional salt tectonics after 101 Ma and before 80 Ma, with E–W extension alternating with N–S extension; (2) NNW–SSE to NNE–SSW compression between 67 and 60 Ma likely related to the far-field transfer of orogenic stress from the Africa–Eurasia plate boundary; (3) E–W compression mainly related to the mid-Atlantic ridge push from 15 Ma onwards. We suggest that the sedimentary cover was decoupled from the crust during salt tectonics and then recoupled from the late Cretaceous onwards, leading to a complex stress history. Our results suggest that during its long-lasting, post-rift geological evolution, the west African passive margin underwent the combined influence of local gravitational stress related to salt tectonics and of far-field tectonic and gravitational lithospheric stress transmitted from distant plate boundaries. These findings may have obvious implications for other passive margins worldwide.

Beyond regional implications, our study reveals the unique potential of the combination of thermometric, geochronological, microstructural and paleopiezometric analyses on cores for the reconstruction of the burial history and paleostress evolution of poorly accessible, deep-buried reservoirs like those located in offshore passive margins. This new information is of prime importance for the understanding and prediction of fracture development, timing of diagenetic cementation, duration of chemical compaction (stylolization), and fluid circulations, hence of carbonate reservoir properties.

Declaration of competing interest

The authors declare that they have no known competing financial interests or personal relationships that could have appeared to influence the work reported in this paper.

Data availability

Data will be made available on request.

Acknowledgments

The authors are very grateful to TotalEnergies for the complete financial support of this research, for providing the cores, and for permission to publish. We would like to thank Philippe Marchina for his help in carrying out the geomechanical tests and for the discussions on the results, and Abel Guihou for his technical support in U–Pb analyses by LA-ICPMS. NEB is funded through the isite-E2S, supported by the ANR PIA and the Région Nouvelle-Aquitaine. The laser UPb dating analyses were carried out as part of the CEREGE-Total Energies collaborative R&D project DATCARB (2018–2021), co-funded by the “Excellence Initiative” program of Aix Marseille University A*MIDEX, TotalEnergies, and Sud region. The constructive comments by Laura Giambiagi, Enrique Gomez-Rivas, and an anonymous reviewer helped improve the quality of the manuscript.

Appendix A. Supplementary data

Supplementary data to this article can be found online at <https://doi.org/10.1016/j.marpetgeo.2023.106219>.

References

- Aharonov, E., Katsman, R., 2009. Interaction between pressure solution and clays in stylolite development: insights from modeling. *Am. J. Sci.* 309 (7), 607–632.
- Ala, M.A., Selley, R.C., 1997. The west African coastal basins. In: *Sedimentary Basins of the World*, vol. 3. Elsevier, pp. 173–186.
- Amrouch, K., Lacombe, O., Bellahsen, N., Daniel, J.-M., Callot, J.P., 2010. Stress and strain patterns, kinematics and deformation mechanisms in a basement-cored anticline: sheep Mountain anticline (Wyoming, USA). *Tectonics* 29, TC1005.
- Anka, Z., Seranne, M., Di Primio, R., 2010. Evidence of a large Upper-Cretaceous depocentre across the Continent-Ocean boundary of the Congo-Angola basin. Implications for palaeo-drainage and potential ultra-deep source rocks. *Mar. Petrol. Geol.* 27 (3), 601–611.
- Artyushkov, E.V., 1973. Stresses in the lithosphere caused by crustal thickness inhomogeneities. *J. Geophys. Res.* 78 (32), 7675–7708.
- Bah, B., Beaudoin, N.E., Lacombe, O., Girard, J.P., Gout, C., Godeau, N., Deschamps, P., 2023. Multi-proxy reconstruction of the burial history and porosity evolution of the TOCA carbonate formation in the lower Congo basin (south west Africa). *Mar. Petrol. Geol.*, 106018.
- Bah, B., Lacombe, O., Beaudoin, N., Girard, J.-P., Gout, C., Godeau, N., 2022. Paleoburial and Paleostress History of a Carbonate Syn-Rift Reservoir : Constraints from Inversion of Calcite Twins and Stylolite Roughness in the Toca Formation (Lower Congo Basin, South Atlantic), vol. 2022. EGU General Assembly 2022, Vienna, Austria, pp. 23–27. <https://doi.org/10.5194/egusphere-egu22-13406>. EGU22-13406.
- Barabási, A.L., Stanley, H.E., 1995. *Fractal concepts in surface growth*. Cambridge university press.
- Beaudoin, N., Lacombe, O., 2018. Recent and future trends in paleopiezometry in the diagenetic domain: insights into the tectonic paleostress and burial depth history of fold-and-thrust belts and sedimentary basins. *J. Struct. Geol.* 114, 357–365.
- Baudouy, S., LeGorjus, C., 1991. Sendji field — People’s Republic of Congo, Congo Basin. In: Beaumont, E.A., Foster, N.H. Z (Eds.), *Structural Traps V: AAPG Treatise of Petroleum Geology, Atlas of Oil and Gas Fields*, pp. 121–149.
- Beaudoin, N., Gasparrini, M., David, M.E., Lacombe, O., Koehn, D., 2019. Bedding-parallel stylolites as a tool to unravel maximum burial depth in sedimentary basins: application to Middle Jurassic carbonate reservoirs in the Paris basin, France. *Geological Society of America. Bulletin* 131 (7–8), 1239–1254.
- Beaudoin, N.E., Lacombe, O., Hoareau, G., Callot, J.P., 2022. How the geochemistry of syn-kinematic calcite cement depicts past fluid flow and assists structural interpretations: a review of concepts and applications in orogenic forelands. *Geol. Mag.* 159 (11–12), 2157–2190.
- Beaudoin, N., Lacombe, O., Koehn, D., David, M.E., Farrell, N., Healy, D., 2020a. Vertical stress history and paleoburial in foreland basins unravelled by stylolite roughness paleopiezometry: insights from bedding-parallel stylolites in the Bighorn Basin, Wyoming, USA. *J. Struct. Geol.* 136, 104061.
- Beaudoin, N.E., Labeur, A., Lacombe, O., Koehn, D., Billi, A., Hoareau, G., Boyce, A., John, C.M., Marchegiano, M., Roberts, N.M., Millar, I.L., Clavier, F., Pecheyran, C., Callot, J.P., 2020b. Regional-scale paleofluid system across the Tuscan Nappe–Umbria–Marche Apennine Ridge (northern Apennines) as revealed by mesostructural and isotopic analyses of stylolite–vein networks. *Solid Earth* 11 (4), 1617–1641.
- Beglinger, S.E., Doust, H., Cloetingh, S., 2012. Relating petroleum system and play development to basin evolution: west African South Atlantic basins. *Mar. Petrol. Geol.* 30 (1), 1–25.
- Bertotti, G., de Graaf, S., Bisdorf, K., Oskam, B., Vonhof, H.B., Bezerra, F.H., et al., 2017. Fracturing and fluid-flow during post-rift subsidence in carbonates of the Jandaira Formation, Potiguar Basin, NE Brazil. *Basin Res.* 29 (6), 836–853.
- Bott, M.H.P., 1993. Modelling the plate-driving mechanism. *J. Geol. Soc.* 150 (5), 941–951.
- Bracken, B. R., 1994. Syn-rift lacustrine beach and deltaic sandstone reservoirs- pre-salt (Lower Cretaceous) of Cabinda, Angola, west Africa, in A.J. Lomando, B. C. Schrieber, and P. M. Harris, eds., *Lacustrine Reservoirs and Depositional Systems: SEPM Core Workshop No. 19*, p. 173–200.
- Brice, S.E., Cochran, M.D., Pardo, G., Edwards, A.D., 1982. Tectonics and sedimentation of the South Atlantic Rift Sequence. In *Studies in Continental Margin Geology. AAPG Mem. No. 34*, ed. J. S. Watkins, C. L. Drake, pp. 5–18. Tulsa, Okla: Am. Assoc. Pet. Geol.
- Brognon, G.P., Verrier, G.R., 1966. Oil and geology in cuanza basin of Angola. *AAPG (Am. Assoc. Pet. Geol.) Bull.* 50 (1), 108–158.
- Brownfield, M.E., Charpentier, R.R., 2006. *Geology and Total Petroleum Systems of the West-Central Coastal Province (7203), West Africa*(No. 2207-B). US Geological Survey.
- Burkhard, M., 1993. Calcite twins, their geometry, appearance and significance as stress-strain markers and indicators of tectonic regime: a review. *J. Struct. Geol.* 15 (3–5), 351–368.
- Cainelli, C., Mohriak, W.U., 1999. Some remarks on the evolution of sedimentary basins along the Eastern Brazilian continental margin. *Episodes-News magazine Int. Uni. Geol. Sci.* 22 (3), 206–216.
- Catuneanu, O., Wopner, H., Eriksson, P.G., Cairncross, B., Rubidge, B.S., Smith, R.M.H., Hancox, P.J., 2005. The Karoo basins of south-central Africa. *J. Afr. Earth Sci.* 43 (1–3), 211–253.
- Chaboureaud, A.C., Guillocheau, F., Robin, C., Rohais, S., Moulin, M., Aslanian, D., 2013. Paleogeographic evolution of the central segment of the South Atlantic during Early Cretaceous times: paleotopographic and geodynamic implications. *Tectonophysics* 604, 191–223.

- Craddock, J.P., Jackson, M., van der Pluijm, B.A., Versical, R.T., 1993. Regional shortening fabrics in eastern north America: far-field stress transmission from the appalachian-ouachita orogenic belt. *Tectonics* 12 (1), 257–264.
- Covey-Crump, S.J., Schofield, P.F., Oliver, E.C., 2017. Using neutron diffraction to examine the onset of mechanical twinning in calcite rocks. *J. Struct. Geol.* 100, 77–97.
- Delpomdor, F., Tack, L., Pr  at, A., 2008. Microstructures in the Neoproterozoic Tillites Around the Congo River Basin (CRB), Democratic Republic of Congo (DRC): Comparison with the Karoo Tillites from the Dekese Borehole in the CRB. In: In 22nd Colloquium of African Geology (CAG22) & 13th Conference of the Geological Society of Africa (GSAf13), p. 108.
- Delvaux, D., Barth, A., 2010. African stress pattern from formal inversion of focal mechanism data. *Tectonophysics* 482 (1–4), 105–128.
- Duval, B., Cramez, C., Jackson, M.P.A., 1992. Raft tectonics in the Kwanza basin, Angola. *Mar. Petrol. Geol.* 9 (4), 389–404.
- Ebner, M., Koehn, D., Toussaint, R., Renard, F., Schmittbuhl, J., 2009. Stress sensitivity of stylolite morphology. *Earth Planet. Sci. Lett.* 277 (3–4), 394–398.
- Ebner, M., Piazzolo, S., Renard, F., Koehn, D., 2010. Stylolite interfaces and surrounding matrix material: nature and role of heterogeneities in roughness and microstructural development. *J. Struct. Geol.* 32 (8), 1070–1084.
- Ehrenberg, S.N., 2006. Porosity destruction in carbonate platforms. *J. Petrol. Geol.* 29 (1), 41–52.
- Ferrill, D.A., Morris, A.P., Evans, M.A., Burkhard, M., Groshong Jr., R.H., Onasch, C.M., 2004. Calcite twin morphology: a low-temperature deformation geothermometer. *J. Struct. Geol.* 26 (8), 1521–1529.
- Gaullier, V., Brun, J.P., Gue, G., Lecanu, H., 1993. Raft tectonics: the effects of residual topography below a salt de' collement. *Tectonophysics* 228 (3–4), 363–381.
- Godeau, N., Deschamps, P., Guihou, A., Leonide, P., Tendil, A., Gerdes, A., et al., 2018. U-Pb dating of calcite cement and diagenetic history in microporous carbonate reservoirs: case of the Urgonian Limestone, France. *Geology* 46 (3), 247–250.
- Goldstein, R.H., Reynolds, T.J., 1994. Systematics of Fluid Inclusions in Diagenetic Minerals.
- Gomez-Rivas, E., Mart  n-Mart  n, J.D., Bons, P.D., Koehn, D., Griera, A., Trav  , A., et al., 2022. Stylolites and stylolite networks as primary controls on the geometry and distribution of carbonate diagenetic alterations. *Mar. Petrol. Geol.* 136, 105444.
- Guiraud, R., Bosworth, W., 1997. Senonian basin inversion and rejuvenation of rifting in Africa and Arabia: synthesis and implications to plate-scale tectonics. *Tectonophysics* 282 (1–4), 39–82.
- Guiraud, R., Bosworth, W., Thierry, J., Delplanque, A., 2005. Phanerozoic geological evolution of northern and central Africa: an overview. *J. Afr. Earth Sci.* 43 (1–3), 83–143.
- Harris, N.B., 2000. Evolution of the Congo rift basin, west Africa: an inorganic geochemical record in lacustrine shales. *Basin Res.* 12 (3–4), 425–445.
- Heidbach, O., Rajabi, M., Reiter, K., Ziegler, M., 2016. World Stress Map 2016. GFZ Data Services.
- Heine, C., Zoethout, J., M  ller, R.D., 2013. Kinematics of the South Atlantic rift. *Solid Earth* 4 (2), 215–253.
- Hintze, J.L., Nelson, R.D., 1998. Violin plots: a box plot-density trace synergism. *Am. Statistician* 52 (2), 181–184.
- Jamison, W.R., Spang, J.H., 1976. Use of calcite twin lamellae to infer differential stress. *Geol. Soc. Am. Bull.* 87 (6), 868–872.
- Johnston, S.T., 2000. The Cape Fold Belt and Syntaxis and the rotated Falkland Islands: dextral transpressional tectonics along the southwest margin of Gondwana. *J. Afr. Earth Sci.* 31 (1), 51–63.
- Jolivet, L., Faccenna, C., Agard, P., Frizon de Lamotte, D., Menant, A., Sternai, P., Guillocheau, F., 2016. Neo-Tethys geodynamics and mantle convection: from extension to compression in Africa and a conceptual model for obduction. *Can. J. Earth Sci.* 53 (11), 1190–1204.
- Kadima, E., Delvaux, D., Sebagenzi, S.N., Tack, L., Kabeya, S.M., 2011. Structure and geological history of the Congo Basin: an integrated interpretation of gravity, magnetic and reflection seismic data. *Basin Res.* 23 (5), 499–527.
- Koehn, D., Ebner, M., Renard, F., Toussaint, R., Passchier, C.W., 2012. Modelling of stylolite geometries and stress scaling. *Earth Planet. Sci. Lett.* 341, 104–113.
- Koehn, D., Rood, M.P., Beaudoin, N., Chung, P., Bons, P.D., Gomez-Rivas, E., 2016. A new stylolite classification scheme to estimate compaction and local permeability variations. *Sediment. Geol.* 346, 60–71.
- Koehn, D., Koehler, S., Toussaint, R., Ghani, I., Stollhofen, H., 2022. Scaling analysis, correlation length and compaction estimates of natural and simulated stylolites. *J. Struct. Geol.*, 104670.
- Kounov, A., Viola, G., De Wit, M., Andreoli, M.A.G., 2009. Denudation along the Atlantic passive margin: new insights from apatite fission-track analysis on the western coast of South Africa. *Geol. Soc. London Special Publ.* 324 (1), 287–306.
- Kulikowski, D., Amrouch, K., 2017. Combining geophysical data and calcite twin stress inversion to refine the tectonic history of subsurface and offshore provinces: a case study on the Cooper-Eromanga Basin, Australia. *Tectonics* 36, 515–541.
- Labeur, A., Beaudoin, N.E., Lacombe, O., Emmanuel, L., Petracchini, L., Da  ron, M., et al., 2021. Burial-deformation history of folded rocks unraveled by fracture analysis, stylolite paleopiezometry and vein cement geochemistry: a case study in the Cingoli Anticline (Umbria-Marche, Northern Apennines). *Geosciences* 11 (3), 135.
- Lacombe, O., Angelier, J., Laurent, P., Bergerat, F., Tourn  ret, C., 1990. Joint analyses of calcite twins and fault slips as a key for deciphering polyphase tectonics: burgundy as a case study. *Tectonophysics* 182 (3–4), 279–300.
- Lacombe, O., Laurent, P., 1992. Determination of principal stress magnitudes using calcite twins and rock mechanics data. *Tectonophysics* 202 (1), 83–93.
- Lacombe, O., Laurent, P., 1996. Determination of deviatoric stress tensors based on inversion of calcite twin data from experimentally deformed monophase samples: preliminary results. *Tectonophysics* 255 (3–4), 189–202.
- Lacombe, O., 2007. Comparison of paleostress magnitudes from calcite twins with contemporary stress magnitudes and frictional sliding criteria in the continental crust: mechanical implications. *J. Struct. Geol.* 29 (1), 86–99.
- Lacombe, O., Amrouch, K., Mouthereau, F., Dissez, L., 2007. Calcite twinning constraints on late Neogene stress patterns and deformation mechanisms in the active Zagros collision belt. *Geology* 35 (3), 263–266.
- Lacombe, O., 2010. Calcite twins, a tool for tectonic studies in thrust belts and stable orogenic forelands. *Oil & Gas Sci. Tech. Revue d'IFP Energ. Nouvelles* 65 (6), 809–838.
- Lacombe, O., Parlangeau, C., Beaudoin, N.E., Amrouch, K., 2021a. Calcite twin formation, measurement and use as stress-strain indicators: a review of progress over the last decade. *Geosciences* 11 (11), 445.
- Lacombe, O., Beaudoin, N., Hoareau, G., Labeur, A., Pecheyran, C., Callot, J.P., 2021b. Dating folding beyond folding, from layer-parallel shortening to fold tightening, using mesostructures : lessons from the Apennines, Pyrenees and Rocky Mountains. *Solid Earth* 12 (10), 2145–2157.
- Laurent, P., Kern, H., Lacombe, O., 2000. Determination of deviatoric stress tensors based on inversion of calcite twin data from experimentally deformed monophase samples. Part II. Axial and triaxial stress experiments. *Tectonophysics* 327 (1–2), 131–148.
- Lehner, P., De Ruiter, P.A.C., 1977. Structural history of atlantic margin of Africa. AAPG (Am. Assoc. Pet. Geol.) Bull. 61 (7), 961–981.
- Lock, B.E., 1980. Flat-plate subduction and the Cape Fold Belt of South Africa. *Geology* 8 (1), 35–39.
- Mahatsente, R., Coblenz, D., 2015. Ridge-push force and the state of stress in the Nubia-Somalia plate system. *Lithosphere* 7 (5), 503–510.
- Mart  n-Mart  n, J.D., Gomez-Rivas, E., G  mez-Gras, D., Trav  , A., Ameneiro, R., Koehn, D., Bons, P.D., 2018. Activation of stylolites as conduits for overpressured fluid flow in dolomitized platform carbonates. *Geol. Soc. London Special Publ.* 459 (1), 157–176.
- Marton, L.G., Tari, G.C., Lehmann, C.T., 2000. Evolution of the Angolan passive margin, West Africa, with emphasis on post-salt structural styles. *Geophys. Monograph Am. Geophysical Union* 115, 129–150.
- Medvedev, S., 2016. Understanding lithospheric stresses: systematic analysis of controlling mechanisms with applications to the African Plate. *Geophys. J. Int.* 207 (1), 393–413.
- Moungoungui, M.M., Guiraud, M., 2009. Neocomian to early aptian syn-rift evolution of the normal to oblique-rifted north Gabon margin (interior and N'komi basins). *Mar. Petrol. Geol.* 26 (6), 1000–1017.
- McGinnis, J.P., Driscoll, N.W., Karner, G.D., Brumbaugh, W.D., Cameron, N., 1993. Flexural response of passive margins to deep-sea erosion and slope retreat: implications for relative sea-level change. *Geology* 21 (10), 893–896.
- Meyers, M.A., V  hringer, O., Lubarda, V.A., 2001. The onset of twinning in metals: a constitutive description. *Acta Mater.* 49 (19), 4025–4039.
- Moulin, M., 2003. *Etude g  ologique et g  ophysique des marges continentales passives: exemple du Za  ire et de l'Angola* (Doctoral dissertation, Universit   de Bretagne Occidentale).
- Moulin, M., Aslanian, D., Unternehr, P., 2010. A new starting point for the South and equatorial Atlantic Ocean. *Earth Sci. Rev.* 98 (1–2), 1–37.
- Newman, J., 1994. The influence of grain size and grain size distribution on methods for estimating paleostresses from twinning in carbonates. *J. Struct. Geol.* 16 (12), 1589–1601.
- Nkodia, H.V., Miyouna, T., Delvaux, D., Boudzoumou, F., 2020. Flower structures in sandstones of the Paleozoic Inkisi Group (Brazzaville, Republic of Congo): evidence for two major strike-slip fault systems and geodynamic implications. *S. Afr. J. Geol.* 123 (4), 531–550.
- N  rnberg, D., M  ller, R.D., 1991. The tectonic evolution of the South atlantic from late jurassic to present. *Tectonophysics* 191 (1–2), 27–53.
- Parlangeau, C., Lacombe, O., Schueller, S., Daniel, J.M., 2018. Inversion of calcite twin data for paleostress orientations and magnitudes: a new technique tested and calibrated on numerically-generated and natural data. *Tectonophysics* 722, 462–485.
- Parlangeau, C., Dimanov, A., Lacombe, O., Hallais, S., Daniel, J.M., 2019. Uniaxial compression of calcite single crystals at room temperature: insights into twinning activation and development. *Solid Earth* 10 (1), 307–316.
- Pascal, C., Cloetingh, S.A., 2009. Gravitational potential stresses and stress field of passive continental margins: insights from the south-Norway shelf. *Earth Planet. Sci. Lett.* 277 (3–4), 464–473.
- Penge, J., Munns, J.W., Taylor, B., Windle, T.M.F., 1999. Rift-raft Tectonics: Examples of Gravitational Tectonics from the Zechstein Basins of Northwest Europe. In: *Geological Society. In: Petroleum Geology Conference Series*, vol. 5. Geological Society of London, London, pp. 201–213. No. 1.
- Perrier, R., Quiblier, J., 1974. Thickness changes in sedimentary layers during compaction history; methods for quantitative evaluation. AAPG Bull. 58 (3), 507–520.
- Rabinowitz, P.D., LaBrecque, J., 1979. The mesozoic South Atlantic ocean and evolution of its continental margins. *J. Geophys. Res. Solid Earth* 84 (B11), 5973–6002.
- Raynaud, S., Carrio-Schaffhauser, E., 1992. Rock matrix structures in a zone influenced by a stylolite. *J. Struct. Geol.* 14 (8–9), 973–980.
- Renard, F., Schmittbuhl, J., Gratier, J.P., Meakin, P., Merino, E., 2004. Three-dimensional roughness of stylolites in limestones. *J. Geophys. Res. Solid Earth* 109 (B3).
- Roberts, N.M., Drost, K., Horstwood, M.S., Condon, D.J., Chew, D., Drake, H., et al., 2020. Laser ablation inductively coupled plasma mass spectrometry (LA-ICP-MS)

- U–Pb carbonate geochronology: strategies, progress, and limitations. *Geochronology* 2 (1), 33–61.
- Rocher, M., Lacombe, O., Angelier, J., Deffontaines, B., Verdier, F., 2000. Cenozoic folding and faulting in the south Aquitaine Basin (France): insights from combined structural and paleostress analyses. *J. Struct. Geol.* 22 (5), 627–645.
- Rocher, M., Lacombe, O., Angelier, J., Chen, H.-W., 1996. Mechanical twin sets in calcite as markers of recent collisional events in a fold-and-thrust belt : evidence from the reefal limestones of southwestern Taiwan. *Tectonics* 15 (5), 984–996.
- Rolland, A., Toussaint, R., Baud, P., Schmittbuhl, J., Conil, N., Koehn, D., et al., 2012. Modeling the growth of stylolites in sedimentary rocks. *J. Geophys. Res. Solid Earth* 117 (B6).
- Rolland, A., Toussaint, R., Baud, P., Conil, N., Landrein, P., 2014. Morphological analysis of stylolites for paleostress estimation in limestones. *Int. J. Rock Mech. Min. Sci.* 67, 212–225.
- Rosenbaum, G., Lister, G.S., Duboz, C., 2002. Relative motions of Africa, Iberia and Europe during alpine orogeny. *Tectonophysics* 359 (1–2), 117–129.
- Rowan, M.G., Tilton, J., Lebit, H., Fiduk, J.C., 2022. Thin-skinned extensional salt tectonics, counterregional faults, and the Albian Gap of Brazil. *Marine and Petroleum Geology* 137, 105478.
- Rowe, K.J., Rutter, E.H., 1990. Palaeostress estimation using calcite twinning: experimental calibration and application to nature. *J. Struct. Geol.* 12 (1), 1–17.
- Rouby, D., Raillard, S., Guillocheau, F., Bouroulec, R., Nalpas, T., 2002. Kinematics of a growth fault/raft system on the West African margin using 3-D restoration. *J. Struct. Geol.* 24 (4), 783–796.
- Salomon, E., Koehn, D., Passchier, C., Hackspacher, P.C., Glasmacher, U.A., 2015. Contrasting stress fields on correlating margins of the South Atlantic. *Gondwana Res.* 28 (3), 1152–1167.
- Sapin, F., Ringenbach, J.C., Clerc, C., 2021. Rifted margins classification and forcing parameters. *Sci. Rep.* 11 (1), 1–17.
- Schmittbuhl, J., Renard, F., Gratier, J.P., Toussaint, R., 2004. The roughness of stylolites: implications of 3D high-resolution topography measurements. *Phys. Rev. Lett.* 93 (23), 238501.
- Séranne, M., Anka, Z., 2005. South Atlantic continental margins of Africa: a comparison of the tectonic vs climate interplay on the evolution of equatorial west Africa and SW Africa margins. *J. Afr. Earth Sci.* 43 (1–3), 283–300.
- Tack, L., Delvaux, D., Kadima, E., Delpomdor, F., Tahon, A., Dumont, P., et al., 2008. The 1.000 M Thick Redbeds Sequence of the Congo River Basin (CRB): a Generally Overlooked Testimony in Central Africa of Post-gondwana Amalgamation (550 Ma) and Pre-karoo Break-Up (320 Ma). In: 22nd Colloquium African Geology (CAG22), pp. 86–88.
- Torsvik, T.H., Rouse, S., Labails, C., Smethurst, M.A., 2009. A new scheme for the opening of the South Atlantic Ocean and the dissection of an Aptian salt basin. *Geophys. J. Int.* 177 (3), 1315–1333.
- Tourmeret, C., Laurent, P., 1990. Paleo-stress orientations from calcite twins in the North Pyrenean foreland, determined by the Etchecopar inverse method. *Tectonophysics* 180 (2–4), 287–302.
- Toussaint, R., Aharonov, E., Koehn, D., Gratier, J.P., Ebner, M., Baud, P., et al., 2018. Stylolites: a review. *J. Struct. Geol.* 114, 163–195.
- Tullis, T.E., 1980. The use of mechanical twinning in minerals as a measure of shear stress magnitudes. *J. Geophys. Res. Solid Earth* 85 (B11), 6263–6268.
- Turner, F.J., Griggs, D.T., Heard, H., 1954. Experimental deformation of calcite crystals. *Geol. Soc. Am. Bull.* 65 (9), 883–934.
- Unternehm, P., G. Péron-Pinvidic, G. Manatschal, and E. Sutra (2010), Hyper-extended crust in the South Atlantic: In search of a model, *Pet. Geosci.*, 16, 207–215.
- Vågnes, E., Gabrielsen, R.H., Haremo, P., 1998. Late Cretaceous–Cenozoic intraplate contractional deformation at the Norwegian continental shelf: timing, magnitude, and regional implications. *Tectonophysics* 300 (1–4), 29–46.
- Viola, G., Kounov, A., Andreoli, M.A.G., Mattila, J., 2012. Brittle tectonic evolution along the western margin of South Africa: more than 500 Myr of continued reactivation. *Tectonophysics* 514, 93–114.
- Wiens, D.A., Stein, S., 1983. Age dependence of oceanic intraplate seismicity and implications for lithospheric evolution. *J. Geophys. Res. Solid Earth* 88 (B8), 6455–6468.
- Wiens, D.A., Stein, S., 1985. Implications of oceanic intraplate seismicity for plate stresses, driving forces and rheology. *Tectonophysics* 116 (1–2), 143–162 (r).
- Withjack, M.O., Olsen, P.E., Schlische, R.W., 1995. Tectonic evolution of the Fundy rift basin, Canada: evidence of extension and shortening during passive margin development. *Tectonics* 14 (2), 390–405.
- Wonham, J.P., Cyrot, M., Nguyen, T., Louhouamou, J., Ruau, O., 2010. Integrated approach to geomodelling and dynamic simulation in a complex mixed siliciclastic–carbonate reservoir, N’Kossa field, Offshore Congo. *Geol. Soc. London Special Publ.* 347 (1), 133–163.
- Wright, K., Cygan, R.T., Slater, B., 2001. Structure of the (1014) surfaces of calcite, dolomite and magnesite under wet and dry conditions. *Phys. Chem. Chem. Phys.* 3, 839–844.
- Zhou, S., Sandiford, M., 1992. On the stability of isostatically compensated mountain belts. *J. Geophys. Res. Solid Earth* 97 (B10), 14207–14221.
- Ziegler, P.A., Cloetingh, S., van Wees, J.D., 1995. Dynamics of intra-plate compressional deformation: the Alpine foreland and other examples. *Tectonophysics* 252 (1–4), 7–59.
- Zoback, M.L., 1992. First-and second-order patterns of stress in the lithosphere: the World Stress Map Project. *J. Geophys. Res. Solid Earth* 97 (B8), 11703–11728.